DEPARTMENT OF PHYSICS
UNIVERSITY OF JYVÄSKYLÄ
RESEARCH REPORT No. 11/2003

DECAY SPECTROSCOPY OF HEAVY NUCLEI BEYOND THE PROTON DRIP LINE

BY
HEIKKI KETTUNEN

Academic Dissertation
for the Degree of
Doctor of Philosophy

To be presented, by permission of the
Faculty of Mathematics and Natural Sciences
of the University of Jyväskylä,
for public examination in Auditorium FYS-1 of the
University of Jyväskylä on December 20, 2003
at 12 o'clock noon

Jyväskylä, Finland
December 2003

ISBN 978-951-39-3149-0
URN:ISBN:978-951-39-3149-0

Preface

The work reported in this thesis has been carried out during the years 1998-2003 at the Department of the Physic of the University of Jyväskylä. I want to express my thanks to the whole staff of the Department for the pleasant and friendly working atmosphere. Especially I would like to thank the staff of the mechanical and electronics workshops providing help for my construction works whenever it was needed.

I wish to thank the leader of the RITU group Prof. Matti Leino for his support and the opportunity to carry out this work in his group. I am also very grateful to the leader of the gamma group Prof. Rauno Julin for his guidance and the interest he has been showing to my work. I also would like to thank Dr. Sakari Juutinen for valuable discussions and Dr. Pete Jones for his help with electronics and computers. Thanks go also to the past and present members of the combined gamma – RITU group. It has been a great pleasure to work in such an inspiring group. This successful combination of two groups has provided a unique possibility to extend the field of studies. It has also been a great pleasure to meet a number of colleagues from different countries visiting our group during this work.

The financial support from the University of Jyväskylä and the Graduate School of the Particle and Nuclear Physics are gratefully acknowledged.

Finally, I would like to express my warmest thanks to my parents, brothers and sister for all their support and encouragement.

Jyväskylä, December 2003

Heikki Kettunen

Abstract

The gas-filled recoil separator RITU has been used in decay studies of neutron-deficient nuclei in the vicinity of the $Z = 82$ proton shell closure and beyond the proton drip line. New information on the proton emitting isotopes of Au and Tl was obtained including the identification of a new proton emitter ^{176}Tl and the first observation of the ground state proton and alpha emission in ^{170}Au. In addition, the alpha-decay properties of a number of neutron deficient Pt and Hg isotopes have been measured. The behaviour of low-lying states in ^{191,193,195}At isotopes were studied utilising alpha decay. The level systematics of these nuclei were observed to differ from those observed in the heavier odd-mass astatine isotopes due to the change of ground state deformation from nearly spherical to oblate shape. A new low-lying state associated with an oblate configuration was identified in the corresponding daughter nuclei ^{187,189,191}Bi applying the alpha-gamma coincidence method. In order to realise these studies at the extreme limit of experimental devices, several technical developments at the recoil separator RITU were required.

Contents

1 Introduction

The limits of nuclear binding are of fundamental interest in nuclear physics. It was expected that the proton unbound nuclei, at the proton drip line, will determine this limit for the neutron deficient nuclei. However, especially in higher-Z nuclei, the potential energy barrier caused by the electrostatic interaction and angular momentum between the unbound proton and the core delay the immediate proton emission. This allows the direct observation of the decay and thus, spectroscopic studies of the nuclei beyond the proton drip line that, in a sense, should not even exist.

The first observation of proton radioactivity was made in 1970 from an isomeric state in ^{53}Co [Jac70, Cer70, Cer72], which is proton bound in the ground state. As long as a decade later, the next proton radioactive nucleus ^{151}Lu [Hof82] was discovered. This was the first time proton emission was observed from the ground state. Soon after this discovery two more proton emitters were observed in the same region: proton emission from the ground and the isomeric state of ^{147}Tm [Kle82] and from the ground state of ^{150}Lu [Hof84]. In addition, two proton emitting nuclei, ^{113}Cs and ^{109}I [Fae84, Gil87], were discovered in a new region of the nuclear chart close to ^{100}Sn. After these discoveries it took again a decade before the next proton emitting nuclei (^{146}Tm [Liv93a], ^{156}Ta and ^{160}Re [Pag92, Liv93b]) were observed. Up to date over thirty proton-radioactive nuclei have been identified, with approximately forty proton-emitting ground and isomeric states. In addition to one-proton radioactivity, the first discoveries of two-proton radioactivity, observed in ^{45}Fe, were recently reported [Pfü03, Gio03].

In the present work several Au, Tl, Bi and At isotopes beyond the proton drip line have been studied. In addition, the alpha-decay properties of a number of neutron deficient Pt and Hg isotopes have been measured. The nuclei are marked in figure 1.1 which shows the part of the nuclear chart relevant to the present work (see also figure 2.1). This region lies more than 20 neutrons away from stability, around the $Z = 82$ proton shell closure and the $N = 104$ neutron mid-shell, which is the famous of shape coexistence in atomic nuclei. Presently available experimental facilities and recoil-decay tagging techniques [Sim86, Pau95] have made in-beam gamma-ray spectroscopic measurements possible in the vicinity and even in this region of the nuclear chart [Jul01] (^{171}Au [Bäc03], ^{187,189}Bi [Hür], ^{191}Bi [Nie03]). However, the decreasing production rates of more neutron-deficient isotopes in heavy-ion induced fusion reactions hinder in-beam gamma-ray spectroscopic measurements. Thus, proton emission and alpha decay provide often the only viable tools to obtain spectroscopic information about these most neutron-deficient heavy nuclei.

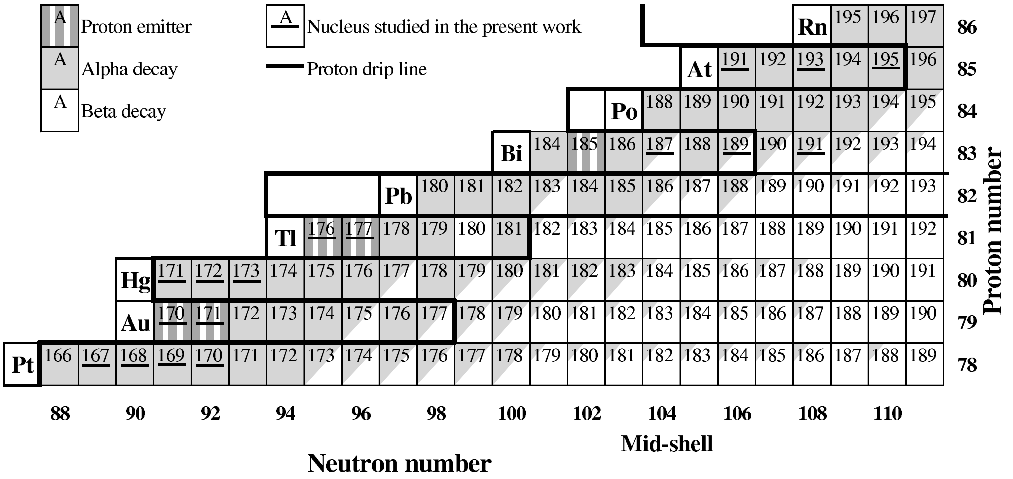

Figure 1.1: A part of the nuclear chart relevant to the present work. The nuclei studied in the present work are underlined. The proton drip line is marked with the thick line. Data for odd-Z nuclei are take from [Aud97, Nov02] and the present work and for even-Z nuclei from [Lir76].

Although the odd-Z nuclei studied in the present work lie beyond the proton drip line, alpha decay is the dominating decay mode for most of them. In this region of the nuclear chart the Q-value of proton emission has to be at least 1 MeV before proton emission is able to compete with alpha decay. This means, that for a particular element there exist several proton unbound isotopes which can be studied via alpha decay, since proton emission is too slow to be detected. For example, in Au isotopes proton radioactivity is not observed until in the seventh isotope beyond the proton drip line and in At isotopes no proton radioactivity was observed even in the fifth proton unbound isotope. Due to the variety of spectroscopic information, that can be obtained via proton emission, the search for the proton-radioactive nuclei is an attractive challenge. The theories of this fairly simple decay process have been developed remarkably during the last years so that in addition to the probing of the mass surface, proton emission can be used to deduce the single-particle structures and shapes of the nuclei beyond the proton drip line.

One motivation for the present studies of the neutron-deficient odd-mass astatine isotopes was to solve the confusion related to the alpha decay of ^{195}At. Due to the summing of the alpha particle energy with the subsequent conversion electron energy in a silicon detector, the decay energy spectrum of ^{195}At is rather complicated. In the present work the alpha-decay scheme of ^{195}At is clarified utilising the alpha-gamma coincidence method. In addition, a new low-lying excited state was found in the corresponding daughter nucleus ^{191}Bi. The decay studies were continued in ^{193}At and ^{191}At to investigate whether the decay schemes of these nuclei are similar to that obtained for ^{195}At. In addition, the possibility for the observation of proton emission in ^{191}At was seriously considered. New information on the low-lying levels in the corresponding daughter nuclei ^{189}Bi and ^{187}Bi was also obtained in these experiments.

All the experiments discussed in the present work were performed at the Accelerator Laboratory of the University of Jyväskylä. The ion beams produced in the ECR ion source [Ärj90, Koi01] were accelerated and delivered to the target by the $K = 130$ MeV cyclotron [Liu92, Hei95]. The spectroscopic measurements of the heavy-ion induced fusion evaporation products were performed using the gas-filled recoil separator RITU [Lei95a]. Before these studies near the limit of nuclear binding were possible, several improvements of the recoil separator RITU were undertaken.

The author of this thesis has developed, designed, constructed and operated the focal plane detector system described in this thesis. The modifications to the RITU dipole chamber and beam stop were designed and constructed by the author. The author has written the enclosed papers. The analysis, interpretations and conclusions were performed by the author. The author proposed and was responsible for the experiments described in the enclosed articles.

I. Investigations into the alpha decay of ^{195}At
H. Kettunen, T. Enqvist, M. Leino, K. Eskola, P.T. Greenlees, K. Helariutta, P. Jones, R. Julin, S. Juutinen, H. Kankaanpää, H. Koivisto, P. Kuusiniemi, M. Muikku, P. Nieminen, P. Rahkila and J. Uusitalo,
Eur. Phys. J. A **16**, 457-467 (2003).

II. Alpha-decay studies of the new isotopes ^{191}At and ^{193}At
H. Kettunen, T. Enqvist, T. Grahn, P.T. Greenlees, P. Jones, R. Julin, S. Juutinen, A. Keenan, P. Kuusiniemi, M. Leino, A.-P. Leppänen, P. Nieminen, J. Pakarinen, P. Rahkila and J. Uusitalo,
Eur. Phys. J. A **17**, 537-558 (2003).

III. Decay studies of ^{170,171}Au, ^{171,172,173}Hg and ^{176}Tl
H. Kettunen, T. Enqvist, T. Grahn, P.T. Greenlees, P. Jones, R. Julin, S. Juutinen, A. Keenan, P. Kuusiniemi, M. Leino, A.-P. Leppänen, P. Nieminen, J. Pakarinen, P. Rahkila and J. Uusitalo,
submitted for publication.

2 Physics background

In the present work the spectroscopic properties of heavy nuclei beyond the proton drip line were studied mainly via alpha decay and proton emission. In order to compare the similarities and differences of these charged particle emissions some of the basic formalisms are presented. An important application in the probing of the nuclear structures was also the alpha-gamma coincidence method which is briefly presented later in section 3.3.4. In the last part of the present section the general properties of neutron-deficient nuclei around the lead region are discussed. But first the basic features of nuclei at the proton drip line are introduced.

2.1 Proton and neutron drip lines

Early nuclear mass models already predicted that certain compositions of protons and neutrons will be energetically unbound with respect to emission of a single nucleon. It was deduced that for each element there would be a maximum and minimum number of neutrons the element could contain without decaying by nucleonic emission. A sufficient surplus of neutrons would lead to the last neutron having a positive binding energy which will thus result in spontaneous neutron emission. This limit defines the neutron drip line. Correspondingly, a lack of neutrons leads to proton unbound nuclei which define the proton drip line.

The conditions that cause the proton and neutron drip lines can be briefly examined based on the semi-empirical mass formula developed by C. F. von Weizsäcker [Wei35] and presented in the following equations

$$M = ZM_H + NM_n - \frac{1}{c^2}B(Z,A) \tag{2.1}$$

$$B(Z,A) = a_{vol}A - a_{surf}A^{\frac{2}{3}} - a_{Coul}\frac{Z^2}{A^{\frac{1}{3}}} - a_{sym}\frac{(N-Z)^2}{A} - \delta(Z,N) \tag{2.2}$$

Here M_H and M_n are the atomic masses of the ^{1}H atom and the neutron, respectively, and $\delta(Z,N)$ is the pairing term, which is defined as

$$\delta(Z,A) = \begin{cases} -a_{pair}A^{-\frac{3}{4}} & \text{if Z and N are even} \\ 0 & \text{if A is odd} \\ a_{pair}A^{-\frac{3}{4}} & \text{if Z and N are odd} \end{cases}$$

The values of the empirical constants used in the present examination are taken from reference [Kra88].

$a_{vol} = 15.5\,\mathrm{MeV}$	volume term
$a_{surf} = 16.8\,\mathrm{MeV}$	surface term
$a_{Coul} = 0.72\,\mathrm{MeV}$	Coulomb repulsion
$a_{sym} = 23.0\,\mathrm{MeV}$	symmetric term
$a_{pair} = 34.0\,\mathrm{MeV}$	pairing effect

On the neutron-rich side of the nuclear chart far from beta stability the largest effect which leads to the break up of the nuclei arises from the asymmetry between the proton and the neutron numbers. This asymmetry is clearly visible in the chart of nuclides shown in figure 2.1. Thus a neutron-rich nucleus becomes neutron unbound when the loss in binding energy $B(Z,A)$, caused by the symmetry term, overcomes the gain due to the volume term when moving to the next heavier isotope of a particular element. Correspondingly, the effect of the symmetry term is not so significant in neutron-deficient nuclei, since the proton drip line lies quite close to the $Z = N$ symmetry line. In fact, the proton drip line crosses the symmetry line around $Z = 50$ nuclei. Therefore the symmetry term contributes to the proton emission in the nuclei below $Z = 50$ and tends to hinder the proton emission in the nuclei above $Z = 50$. It is the Coulomb repulsion between the positively charged protons which mainly causes the proton emission in neutron-deficient nuclei. In addition, the Coulomb effect pushes the proton drip line much closer to the stable nuclei in comparison to the corresponding neutron drip line on the neutron-rich side. The proton and neutron drip lines calculated for odd-A nuclei using equation 2.2 are shown in figure 2.1. It should be noted that the semi-empirical mass formula does not take into account nuclear shell structural effects which may affect the positions of the calculated drip lines. Much more sophisticated and accurate mass formulae, which include also the nuclear shell effects and further details, can be found in the collections of publications listed in references [Mar76, Hau88] and in reference [Möl95].

A striking feature at the proton drip line is the variation on its position between the odd-Z and even-Z nuclei. This is illustrated in figure 1.1 where a part of the proton drip line is drawn in more detail. In the even-Z nuclei the proton drip line is shifted approximately ten neutrons further from the

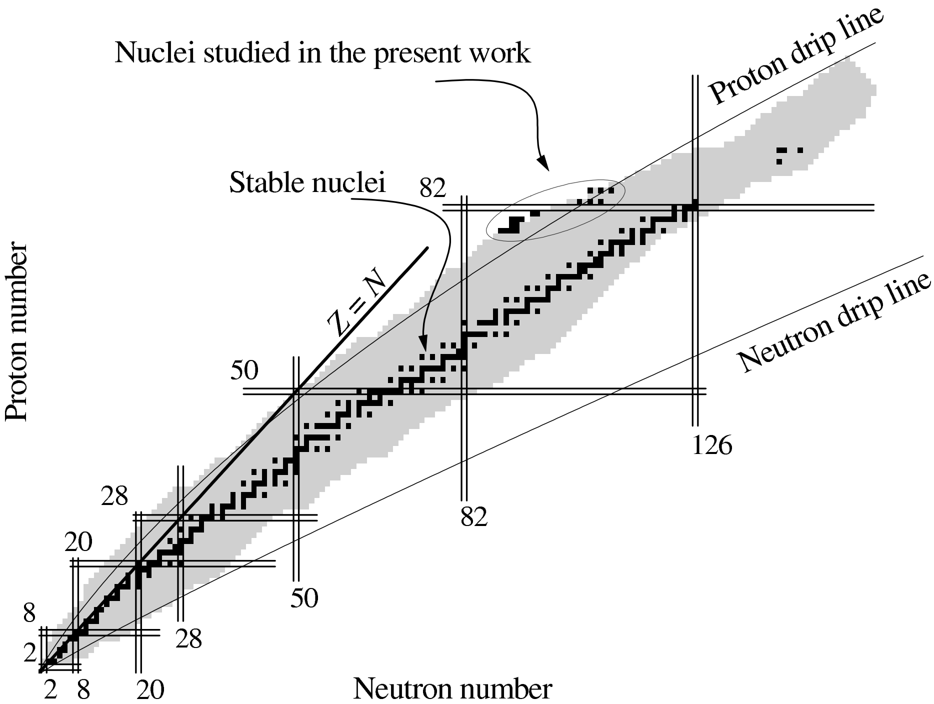

Figure 2.1: The chart of nuclei. The line of black squares represents the stable nuclei. The black squares inside the ellipse represent the nuclei studied in the present work. The shaded area shows experimentally observed nuclei. The proton and neutron drip lines for odd-A nuclei are calculated using equation 2.2.

stability due to the stabilising effect of proton pairing.

In general, the Coulomb repulsion causes the charged particle emission. On the other hand, the Coulomb force also slows down the process so that the direct observation of charged particle emission is possible. This is because the particle has to penetrate through the potential energy barrier before it can escape from the nucleus. Thus, the proton emission half-life of proton unbound nuclei may reach up to infinity, as compared with typical life time for proton unbound resonances which are on the order of 10^{-18} seconds. In light nuclei (below $Z = 20$) the Coulomb barrier is not high enough to delay the proton emission and only very short-lived proton unbound resonances can be expected to occur in these nuclei. In heavier nuclei (especially above $Z = 50$) the Coulomb barrier is higher and its effect on the proton emission half-life is significant. Thus, the Coulomb effect smears out the proton drip line so that more than one proton emitting isotope can be observed for a particular element. For example, four proton emitting isotopes *i.e.* ^{164}Ir [Ket01a, Mah02] and $^{165-167}$Ir [Dav97] have been identified for iridium.

2.2 Alpha decay

Many of the heavy nuclei decay via alpha particle emission. This sub-barrier process can be illustrated by the formula

$$ {}^{A}_{Z}X_{N} \rightarrow {}^{A-4}_{Z-2} X'_{N-2} + \alpha \tag{2.3}$$

where *X* and *X'* represent the mother and daughter nuclei and α is the nucleus of a ^{4}He-atom. The other decay modes where a nucleon or cluster of nucleons is emitted are very rare. The main reason why alpha decay is so common in the region of heavy nuclei is that the alpha particle is very tightly bound due to its doubly magic character. Thus the sum mass of the final products is smaller than the mass of the initial nucleus, which makes the alpha decay energetically favourable.

2.2.1 Alpha-decay Q-value

A necessary condition for spontaneous alpha decay or any decay is, that the mass of the initial nucleus is greater than the sum mass of the final products. In other words, the Q-value of the decay has to be greater than zero. Using atomic masses, the alpha decay Q_α-value can be calculated using the equation

$$Q_\alpha = (M_m - M_d - M_{He})c^2 \tag{2.4}$$

where M_m, M_d and M_{He} are the atomic masses of the mother and daughter nuclei and the ^{4}He atom, respectively.

The Q_α-value represents the total kinetic energy of the decay fragments which is the sum of the kinetic energies of the alpha particle E_α and the daughter nucleus E_d. According to the conservation of linear momentum the total kinetic energy of the system is divided between the alpha particle and the daughter nucleus in inverse proportion to their masses. Thus the experimental alpha-decay Q_α-value, corresponding to the value in equation 2.4, is obtained from the measured alpha-particle energy E_α as

$$Q_\alpha = E_\alpha + E_d = E_\alpha(1 + \frac{M_{He}}{M_d}) \approx E_\alpha(1 + \frac{4}{A_d}) \tag{2.5}$$

where A_d is the mass number of the daughter nucleus. Combining this equation with equation 2.4, alpha decay can be used to measure atomic masses. If the absolute mass of any atom occurring in the alpha-decay chain is known, the masses of the other atoms can be calculated by applying the above equations.

The Q_α-value presented above is, however, somewhat different than what would be obtained if dealing with electron bare nuclei. This is because the alpha particle loses some energy when it moves through the electron cloud surrounding the daughter nucleus. This screening correction E_{sc} for alpha decay is discussed in references [Per57, Ras66] and given as

$$E_{sc} = 65.3 \cdot Z^{7/5} - 80 \cdot Z^{2/5} \quad [eV] \tag{2.6}$$

where Z is the proton number of the daughter nucleus. Thus the Q_α^{bare}-value of an electron bare nucleus is obtained from the measured alpha-particle energy according to the equation

$$Q_\alpha^{bare} \approx E_\alpha(1 + \frac{4}{A_d}) + E_{sc} \tag{2.7}$$

2.2.2 Simple theory for alpha decay

One striking feature of alpha decay is the predictable dependence between the decay energy and the half-life. The higher is the decay energy, the shorter is the half-life. This feature was noticed by Geiger and Nuttall (Geiger-Nuttall rule) soon after Rutherford discovered the existence of the atomic nucleus in 1911. The dependence is so smooth, especially in even-even nuclei, that it can be described by a fairly simple semi-empirical formula developed by Taagepera and Nurmia [Taa61]

$$log_{10}T_{1/2} = 1.61(Z \cdot E_\alpha^{-1/2} - Z^{2/3}) - 28.9 \tag{2.8}$$

In the equation, $T_{1/2}$ is given in years, Z is the atomic number of the daughter nucleus and E_α is the kinetic energy of the alpha particle in MeV. The very sensitive relation between the alpha-decay energy and the half-life can be easily noticed by examining the equation. A factor of two change in the alpha-decay energy corresponds to a change of 15 to 20 magnitudes in half-life, depending on the atomic number and decay energy.

For a better understanding and to obtain accurate half-life predictions, quantum mechanics is applied to examine the alpha-decay process. The first theory was developed as long ago as 1928 almost simultaneously by Gamow and by Gurney and Condon. In the theory a preformed alpha particle is assumed to move inside the daughter nucleus and to knock, with frequency f, against the walls of the spherical potential barrier *V(r)*. The potential barrier, shown in figure 2.2, is caused by the Coulomb interaction between the daughter nucleus and the alpha particle. Classically, the alpha particle cannot penetrate the potential barrier, to the classically forbidden region between the inner and the outer classical turning points R_i and R_o, respectively. But according to quantum mechanics the alpha particle can tunnel through the potential barrier with the penetration probability P, which can be approximated by applying the WKB-integral over the classically forbidden region of the potential as follows

$$P = exp\Big\{ -2 \int_{R_i}^{R_o} \frac{(2m)^{1/2}}{\hbar} \left[V(r) - Q_\alpha^{bare}\right]^{1/2} dr \Big\} \tag{2.9}$$

In the equation m is the reduced mass which is defined as

$$m = \frac{M_{He} M_d}{M_{He} + M_d} \approx \frac{4 \cdot A_d}{(4 + A_d)} \cdot m_u \tag{2.10}$$

where m_u is the atomic mass unit.

The calculated decay constant λ_{calc} for the alpha decay is obtained as the product of the knocking frequency f and the penetration probability P

$$\lambda_{calc} = \frac{ln2}{T_{1/2}^{calc}} = f \cdot P \quad [1/\mathrm{s}] \tag{2.11}$$

In the original theory the potential barrier *V(r)* was approximated by taking into account only the Coulomb potential outside of the daughter nucleus as shown in figure 2.2. The sharp edge of the potential at the inner classical turning point R_i is a little unrealistic. Also difficulties in the estimation of the knocking frequency f cause some inaccuracies in the prediction. However, the calculation is able to reproduce the measured half-lives within $1-2$ orders of magnitude, which is a good result.

In the present work, the experimental alpha-decay half-lives are compared to theoretical values which were calculated according to the method of Rasmussen [Ras59]. In this calculation the edge of the potential barrier at the surface of the daughter nucleus is smoothed by the superposition of a nuclear potential [Igo58] and the Coulomb potential. Also the centrifugal potential caused by the orbital angular momentum ℓ of the emitted alpha particle is taken into account. The potential used by Rasmussen is then

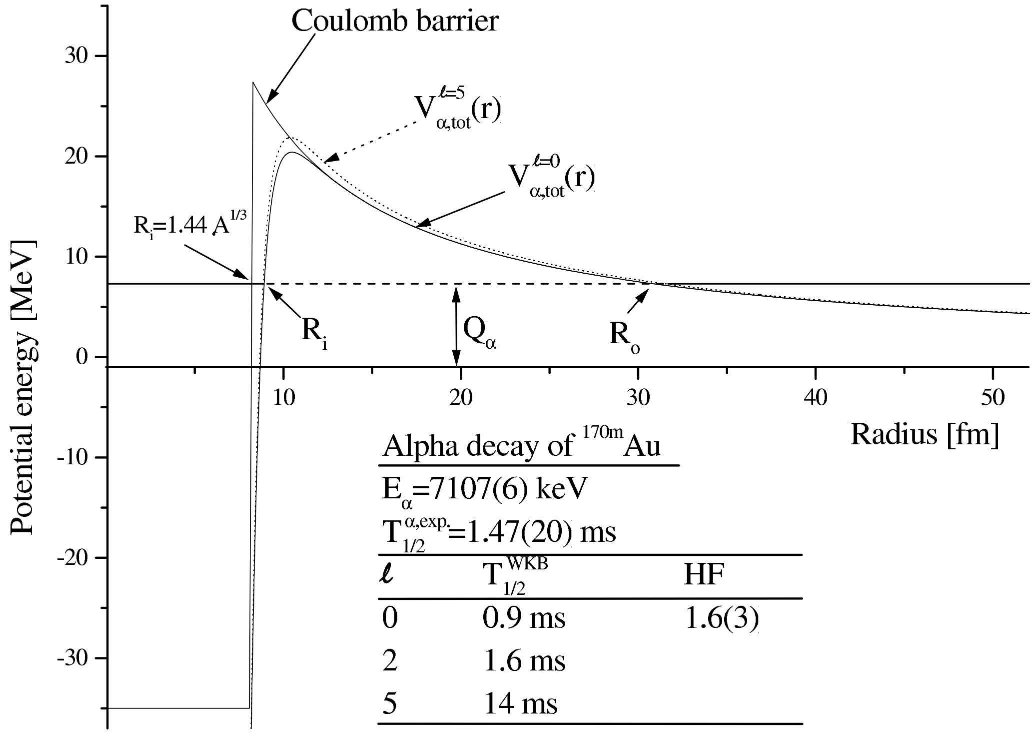

Alpha decay of ^{170m}Au

E_α=7107(6) keV

$T^{\alpha,exp.}_{1/2}$=1.47(20) ms

ℓ	$T^{WKB}_{1/2}$	HF
0	0.9 ms	1.6(3)
2	1.6 ms	
5	14 ms	

Figure 2.2: Representation of the potential used in calculations of the alpha-decay half-life. The inset table shows the calculated partial half-lives and the corresponding hindrance factor for the alpha decay of ^{170m}Au assuming various angular momentum values of the emitted alpha particle. According to the definition of the hindrance factor *HF* the alpha decay corresponds to an unhindered $\ell = 0$ transition.

$$V(r) = -1100 \cdot exp\Big\{ - \left[\frac{r - 1.17 \cdot A^{1/3}}{0.574}\right]\Big\} + \frac{2Ze^2}{4\pi\epsilon_o r} + \frac{\hbar^2}{2mr^2}\ell(\ell+1) \quad (2.12)$$

where A and Z represent the mass and atomic numbers of the daughter nucleus and m is the reduced mass given in equation 2.10. The shape of the potential and the effect of the additional angular momentum barrier is illustrated in figure 2.2 for the alpha decay of ^{170m}Au. The penetration probability P is obtained by substituting the potential *V(r)* to equation 2.9 and by numerical calculation of the integral between the inner and outer classical turning points. In addition, the knocking frequency *f*, needed for the half-life calculation in equation 2.11, is estimated by normalising to a known unhindered alpha decay. Sometimes the frequency is normalised using the alpha-decay properties of even-even nuclei closest to the nucleus of interest. In the present work, the frequency *f* is normalised to the ground-state to ground-state alpha decay of ^{212}Po to the doubly magic ^{208}Pb nucleus.

2.2.3 Hindrance factor and reduced alpha emission width

The compatibility of the theoretically calculated and the measured alpha-decay half-lives can be used to probe the structural differences of the initial and the final states in mother and daughter nuclei, respectively. The traditional quantity to illustrate the properties of the alpha decay is the so called hindrance factor *HF*, which is defined simply as

$$HF = \frac{T_{1/2}^{exp}}{T_{1/2}^{calc}} \tag{2.13}$$

For an unhindered alpha decay the hindrance factor *HF* is less than four. This indicates that the angular momentum ℓ carried away by the emitted alpha particle is zero and the configurations of the initial and the final state are similar. In other words, for an alpha decay with $\ell > 0$ the hindrance factor cannot be less than four (for exceptions see for example doubly magic nuclei in reference [Ako98]). Thus, the alpha decay of ^{170m}Au illustrated in figure 2.2 is concluded to correspond to the $\ell = 0$ transition. For a hindered alpha decay the hindrance factor is usually at least a few tens of units. In these alpha decays, the spins and parities of the initial and the final state (I_i^π and I_f^π) are usually different and the ℓ value of the alpha particle is greater than zero. The allowed angular momentum ℓ carried by the alpha particle is limited to the range $|\mathrm{I}_i - \mathrm{I}_f| \leq \ell \leq (\mathrm{I}_i + \mathrm{I}_f)$ and the parity π has to follow the selection rule $\pi_f = \pi_i(-1)^\ell$. Since the experimental half-life of a hindered alpha decay is significantly longer than the theoretically predicted value, the decay process is not as fast or as probable as in an unhindered alpha decay. It can be thought that the process is slow and hindered, because it requires several steps, such as the rearrangement of proton and neutron configurations before the alpha particle can be emitted.

Another commonly used quantity to illustrate the properties of alpha decay is the reduced alpha emission width δ^2 expressed in the form

$$\delta^2 = \frac{\lambda_{exp} \cdot h}{P} \quad [eV] \tag{2.14}$$

Here λ_{exp} is the experimental alpha-decay constant, h is Planck's constant and P the penetration probability calculated according to the method of Rasmussen [Ras59]. For an unhindered alpha decay the reduced width is typically larger than 40 keV and around 1 keV for a hindered alpha decay. Both the hindrance factor and the reduced width express the speed of the alpha decay compared to the expected value. Since they are both defined based on the same calculation of penetration probability P they are inversely proportional to each other.

2.3 Proton emission

According to the familiar notation the emission of a proton p can be illustrated by the following formula

$$^{A}_{Z}X_{N} \rightarrow ^{A-1}_{Z-1} X'_{N} + p \tag{2.15}$$

The necessary requirement for spontaneous proton emission is naturally a positive Q_p-value. This requirement defines the line of proton unbound nuclei, known as the proton drip line (see section 2.1).

The equations for the proton emission Q_p-value are analogous to the equations presented for alpha decay in section 2.2.1. Hereby, the proton emission Q_p-value can be calculated using the atomic masses of the mother and the daughter nuclei and the hydrogen atom, M_m, M_d and M_H, respectively, as

$$Q_p = (M_m - M_d - M_H)c^2 \tag{2.16}$$

The experimental Q_p and Q_p^{bare} values are obtained from the measured proton energy E_p according to the equations

$$Q_p^{bare} = Q_p + E_{sc} = E_p(1 + \frac{M_H}{M_d}) + E_{sc} \approx E_p(1 + \frac{1}{A_d}) + E_{sc} \tag{2.17}$$

The screening correction E_{sc} for proton emission can be calculated from tabulated neutral-atom electron binding energies given by Huang and Mark [Hua76]. The electron screening corrections needed for the present work are 16.32 keV for Au, 17.01 keV for Tl and 18.45 keV for At isotopes.

Compared to alpha particles, protons experience an approximately factor of two lower Coulomb barrier. Conversely, the angular momentum barrier is approximately four times higher for protons than for alpha particles. This follows from the linear dependence of the Coulomb barrier on the charge of the emitted particle and from the inverse dependence of the angular momentum barrier on its reduced mass. Thus the contribution of the angular momentum barrier to the total potential barrier is much larger for protons than for alpha particles. This makes the half-life of the proton emission extremely sensitive to the angular momentum ℓ of the emitted proton, which has to follow the selection rules of $|\mathrm{I}_i - \mathrm{I}_f| \pm \frac{1}{2} \leq \ell \leq (\mathrm{I}_i + \mathrm{I}_f) \pm \frac{1}{2}$ for the spins and $\pi_f = \pi_i(-1)^{\ell}$ for the parities of the initial and the final states, I_i^{π} and I_f^{π}, respectively. This sensitivity gives an opportunity to obtain direct spectroscopic information on the ordering and structure of the proton orbitals involved in the proton emission by comparing the experimental decay rate to the theoretically predicted values.

2.3.1 Simple theory for proton emission in spherical nuclei

On a simple level, the theoretical examination of the proton emission can be done using a similar treatment as is done for alpha decay. Actually, the theoretical description of the emission of a single nucleon (proton) should be somewhat easier than the description of alpha emission, in which a cluster of four nucleons is emitted. The first simplification arises from the estimation of the knocking frequency f as the proton strikes the potential wall and tries to penetrate it. Instead of normalising the frequency to a measured decay rate (as is done for alpha decay) it can reliably be estimated using the equation

$$f = \frac{\sqrt{2}\pi^2\hbar^2}{m^{3/2}R_c^3(zZe^2/4\pi\epsilon_o R_c - Q_p^{bare})} \quad [1/\mathrm{s}] \tag{2.18}$$

as given in reference [Hof93]. The equation is based on an analogous expression given for the alpha decay of spherical nuclei by Bethe [Bet37] and Rasmussen [Ras66]. In the present examination the theoretical decay constant λ_{calc} for proton emission is obtained by multiplying the knocking frequency f with the potential barrier penetration probability P in a similar manner as was done for alpha decay in equation 2.11. The potential barrier between the proton and the daughter nucleus is taken as a superposition of the nuclear $V_{j\ell}(r)$, the Coulomb $V_C(r)$ and the centrifugal potential $V_\ell(r)$. As suggested in reference [Hof93] the real part of the optical model potential given by Becchetti and Greenlees [Bec69] was used for the nuclear potential $V_{j\ell}(r)$. The parameterisations of the nuclear potential along with the formulae used for the Coulomb and centrifugal potentials are presented in equations $2.19 - 2.26$ taken from reference [Bec69]. The shape of the potential barrier for proton emission in ^{170}Au is shown in figure 2.3. The effect of the angular momentum ℓ of the emitted proton is also illustrated. Compared to the corresponding potential experienced by an alpha particle and shown in figure 2.2 the significance of the centrifugal potential in proton emission is obvious.

$$V_{j\ell}(r) = -V_R f(r, R_R, a_R) + V_{SO}\lambda_\pi^2 \ \overline{\sigma} \cdot \overline{\ell} \ (1/r)(d/dr)[f(r, R_{SO}, A_{SO})] \quad (2.19)$$

$$V_R = \ 54.0 - 0.32 \cdot E_p + 0.4Z/A^{1/3} + 24.0(N - Z)/A \quad [\mathrm{MeV}] \quad (2.20)$$

$$V_C(r) = \frac{zZe^2}{4\pi\epsilon_o r}(3 - \frac{r^2}{R_c^2}) \quad for \quad r \leq R_c \quad (2.21)$$

$$V_C(r) = \frac{zZe^2}{4\pi\epsilon_o r} \quad for \quad r > R_c \quad (2.22)$$

$$V_\ell(r) = \ell(\ell + 1)\frac{\hbar}{2mr^2} \quad (2.23)$$

$$\overline{\sigma} \cdot \overline{\ell} = \ell \quad for \quad j = \ell + 1/2 \quad (2.24)$$

$$\overline{\sigma} \cdot \overline{\ell} = -(\ell + 1) \quad for \quad j = \ell - 1/2 > 0 \quad (2.25)$$

$$f(r, R, a) = \frac{1}{1 + exp\{(r - R)/a\}} \quad (2.26)$$

$\overline{\sigma} \cdot \overline{\ell}$ = scalar product of the intrinsic and orbital angular momentum operators
j, ℓ = total and orbital angular momentum quantum numbers of the emitted particle
z, Z = charge of proton and daughter nucleus
A, N = mass and neutron numbers of daughter nucleus
R_R = 1.17 $\cdot A^{1/3}$ [fm], a_R = 0.75 [fm]
R_{SO} = 1.01 $\cdot A^{1/3}$ [fm], a_{SO} = 0.75 [fm], V_{SO} = 6.2 [MeV]
R_c = 1.21$\cdot$A$^{1/3}$ [fm]
m = reduced mass $\approx \frac{m_p \cdot A}{m_p/m_u + A}$
m_u = 931.501 [MeV/c^2]
m_p = 938.211 [MeV/c^2]
λ_π^2 = pion Compton wavelength squared $\approx$ 2.0 [fm^2]

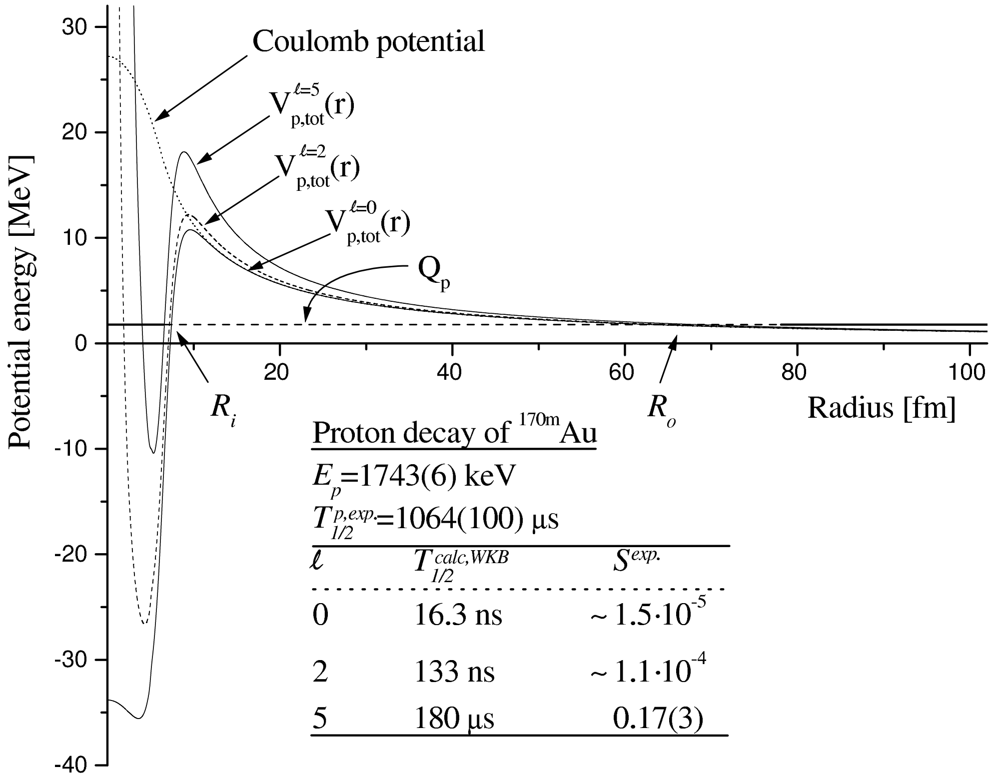

Proton decay of ^{170m}Au

E_p=1743(6) keV

$T_{1/2}^{p,exp.}$=1064(100) µs

ℓ	$T_{1/2}^{calc,WKB}$	$S^{exp.}$
0	16.3 ns	~ $1.5 \cdot 10^{-5}$
2	133 ns	~ $1.1 \cdot 10^{-4}$
5	180 µs	0.17(3)

Figure 2.3: Representation of the potential used in calculations of the proton emission half-life. The inset table shows the calculated proton half-lives and the corresponding experimental spectroscopic factors for proton emission from ^{170m}Au assuming various angular momentum values of the emitted proton.

In analogy with alpha decay the penetration probability P is obtained by integrating over the classically forbidden region of the potential barrier between the classical turning points R_i and R_o,

$$P = exp\Big\{ -2 \int_{R_i}^{R_o} \frac{(2m)^{1/2}}{\hbar} \left[V_{j\ell}(r) + V_C(r) + V_\ell(r) - Q_p^{bare}\right]^{1/2} dr \Big\} \qquad (2.27)$$

During the last few years the theory of proton radioactivity has progressed remarkably leading to a detailed description of the proton emission in spherical as well as in deformed nuclei. An introduction to much more sophisticated theories and to the developments in the theory of proton radioactivity is given in reference [Mag02].

2.3.2 Spectroscopic factor

The calculation of the proton emission half-life based on the WKB approximation presented above is valid only for spherical nuclei. In addition, the calculation does not take into account any nuclear structure effects which may affect the half-life, except the orbital angular momentum of the emitted proton. These nuclear structure effects are taken into account by a spectroscopic factor S_j, which describes the probability to end up to a particular final state in the daughter nucleus by removing an uninteracting proton from orbital (nlj) in the mother nucleus. The theoretical definition of the spectroscopic factor is given as [Boh69]

$$S_j^{th} = \frac{1}{2I_i + 1} |\langle I_i || a_{nlj}^{\dagger} || I_f \rangle|^2 \tag{2.28}$$

Theoretical spectroscopic factors for proton emitting nuclei in the region of $64 < Z < 82$ have been calculated by applying a low-seniority shell-model calculation of the wave function for the mother and daughter state [Dav97]. The calculation was performed for the $3s_{1/2}$, $2d_{3/2}$ and $1h_{11/2}$ proton orbitals whose single-particle energies were assumed to be degenerate. The spectroscopic factors $S(p)$ for the proton emission from odd-Z nuclei to the ground state of the daughter nuclei was observed to be dependent only on the number of proton hole pairs p of the daughter nucleus below the $Z = 82$ proton shell closure as

$$S^{calc}(p) = \frac{p}{9} \quad with \quad 1 \leq p \leq 9 \tag{2.29}$$

Using this formalism, the calculated spectroscopic factors for the proton emission in Tl and Au isotopes, studied in the present work, are 0.11 and 0.22, respectively (compare to the tabulated values in figure 2.3). Another calculation for theoretical spectroscopic factors based on the independent-quasiparticle BCS approach is presented in reference [Åbe97]. The effect of the spectroscopic factor on the proton emission half-life is clarified by the definition of the experimental spectroscopic factor S^{exp}, which is the ratio of the experimental and theoretical half-lives

$$S^{exp} = \frac{T_{1/2,p}^{calc}}{T_{1/2,p}^{exp}} \tag{2.30}$$

Since the theoretical and experimental spectroscopic factors should correspond to each other very closely, it can be expected that the experimental proton emission half-lives are somewhat longer than the values of the WKB approximation calculation for the nuclei in the region of $64 < Z < 82$.

2.4 Neutron-deficient nuclei around lead

The region of neutron-deficient nuclei far from stability around the closed $Z = 82$ proton shell and the $N = 104$ neutron mid-shell offers an interesting challenge for various theoretical models as well as experimental instruments. A variety of nuclear phenomena can be observed in this limited region of the nuclear chart and understood by the coupling of the particles and particle holes to the proton-magic Pb core. In addition, the vicinity of the proton drip line in odd-Z nuclei offers an opportunity to observe proton emission in this region.

Currently, the coexistence of different shapes in the atomic nucleus is an enthusiastically studied topic in nuclear physics. The neutron-deficient lead region offers an excellent opportunity to study this phenomenon in the vicinity of the closed proton shell, see [Jul01] and references therein. The development of different nuclear shapes can be followed from spherical at the $N = 126$ neutron closure to the deformed region around the $N = 104$ neutron mid-shell. One of the theoretical tools to understand the deformed nuclear structures is the deformed shell model or Nilsson model [Mot55, Nil55]. The Nilsson model describes the single-particle motion of a proton or a neutron in an axially symmetric nuclear potential. Originally calculations were based on the modified harmonic oscillator potential but later on more realistic nuclear potentials, such as the deformed Woods-Saxon potential, have been applied. Figure 2.4 shows the development of the single-particle level energies for protons as a function of quadrupole axial deformation in the region around lead ($Z = 82$).

The experimental level systematics of even-mass Pb isotopes, shown in figure 2.5, illustrate the typical features in the mid-shell region, where the deformed structures come down in excitation energy. The closed proton shell in lead nuclei favours a spherical ground state, coexisting with an excited oblate-deformed configuration, associated with the excitation of a proton pair across the closed $Z = 82$ shell gap. Multiparticle and multihole excitations, which are associated with strong prolate deformations, were predicted to occur at an excitation energy comparable to that of the oblate deformed structure near the neutron mid-shell at $N = 104$ [May77, Ben89]. The specific conditions in this particular region of the nuclear chart lead to the existence of a possible unique triple coexistence of different nuclear shapes [All98, And00], at comparable level energies. The even-even platinum and mercury isotopes present even more dramatic examples of down sloping level energies of the deformed structures just below the $Z = 82$ proton shell closure [Woo92, Jul01]. In the platinum isotopes, which are only four protons below the shell closure,

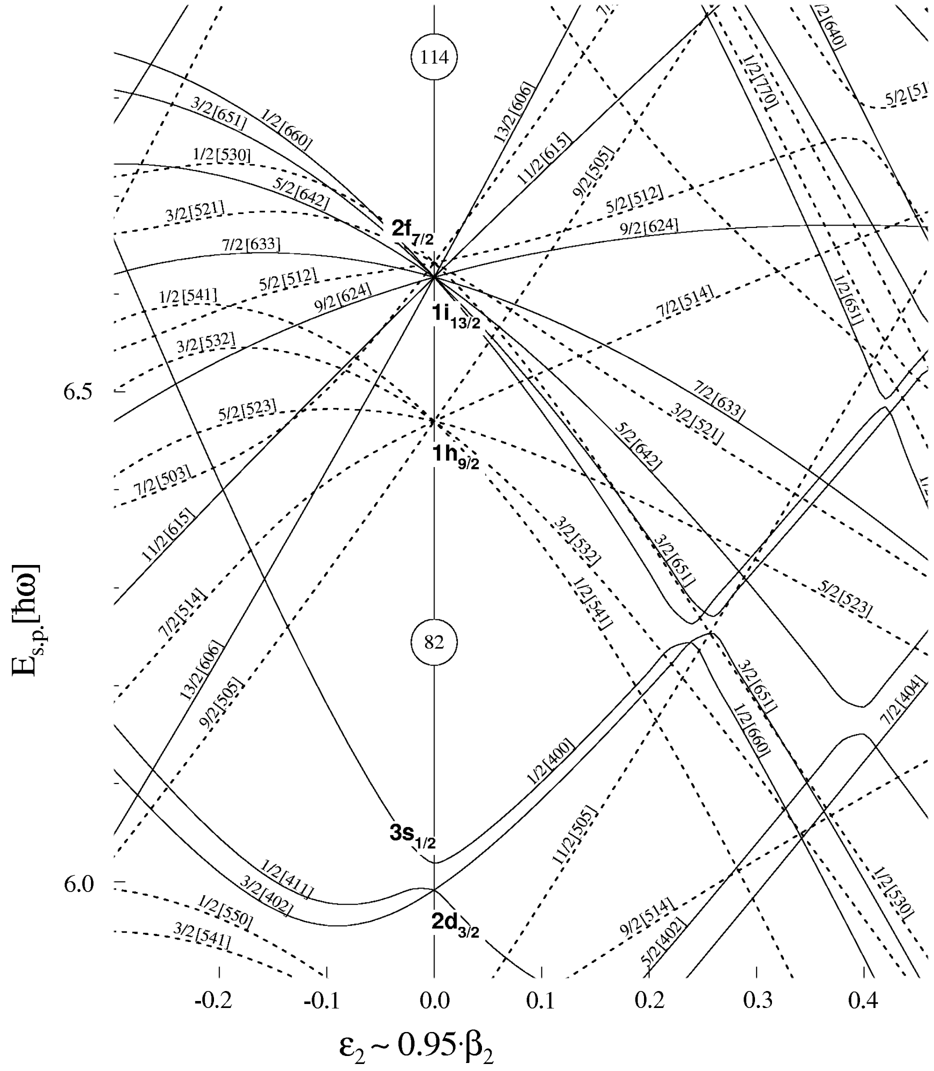

Figure 2.4: Nilsson diagram for protons. The diagram has been taken from reference [Fir96]

the strongly deformed structure becomes the ground state in the mid-shell region.

The competition between different nuclear shapes can also be seen in the level systematics of the neutron-deficient polonium isotopes ($Z = 84$), shown in figure 2.6. Experimental results indicate that the spherical ground state of heavier polonium isotopes transforms to a slightly oblate shape around ^{194}Po and that the oblate shape dominates in the ground state of ^{192}Po and ^{190}Po [Hel99, Vel02]. An alternative approach to the level systematics in ^{194}Po and

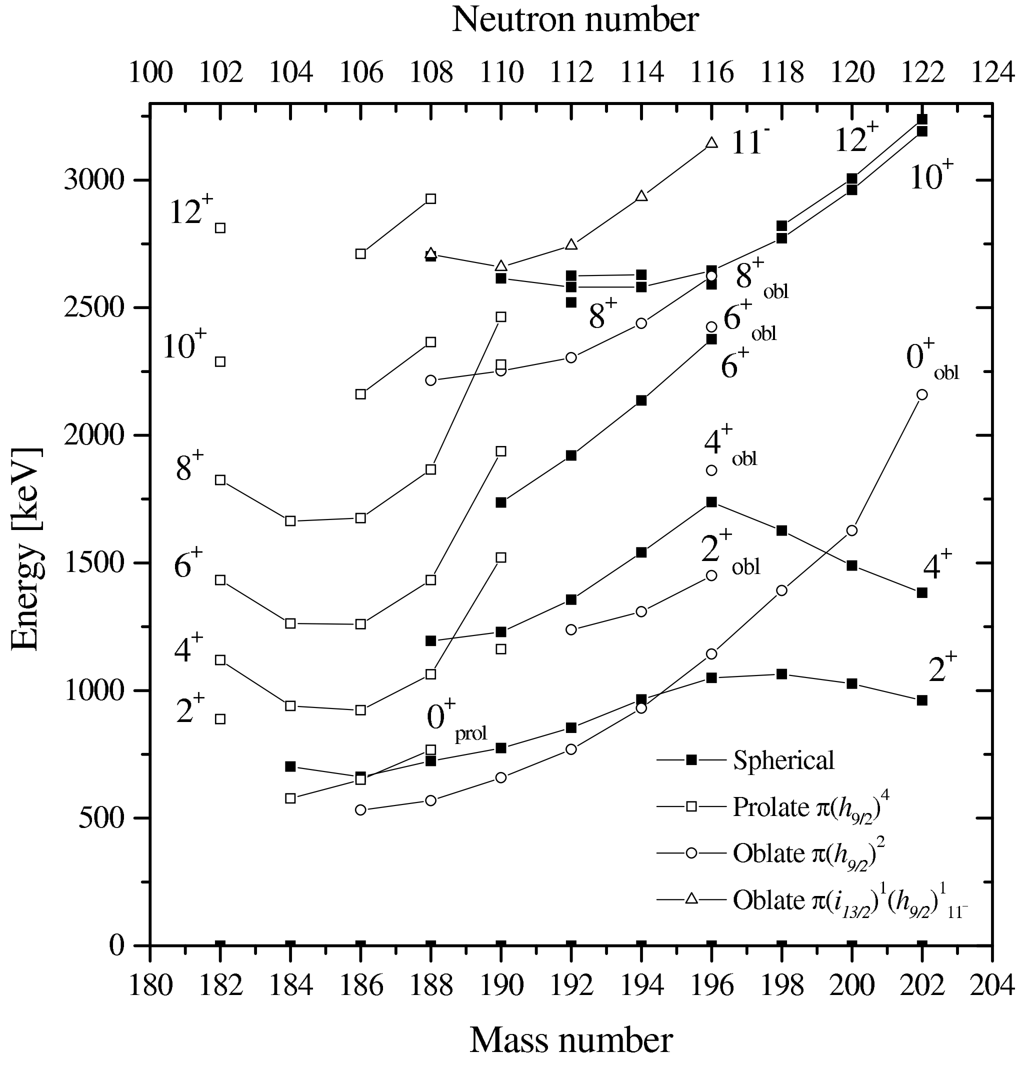

Figure 2.5: Level systematics for even-mass Pb isotopes taken from [Jul01].

^{192}Po base on an anharmonic vibrator interpretation is presented in references [You95, Fot97]. In a recent experiment the prolate deformed intruder configuration was observed to become yrast above I$\geq 4\hbar$ in ^{190}Po [Vel02]. This can be seen as an unexpected drop in the 4$^+$, 6$^+$ and 8$^+$ level energies of ^{190}Po in figure 2.6. Preliminary evidence for the prolate-deformed structure dropping further down in energy and possibly dominating the ground state in ^{188}Po is suggested on the basis of alpha-decay studies [And99]. Properties of neutron-deficient polonium isotopes are predicted quite well by theoretical calculations in reference [May77] and more recently in [Oro99, Smi03].

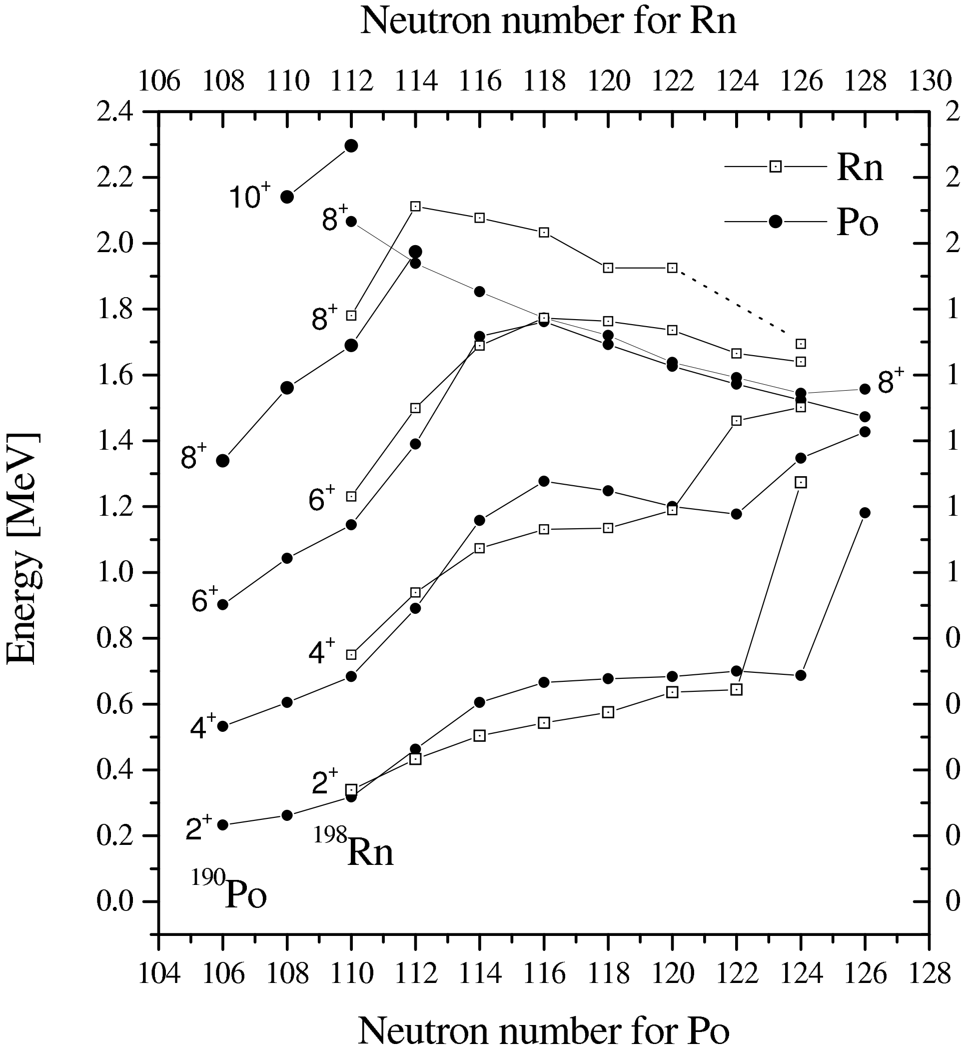

Figure 2.6: Level systematics for even-mass Po and Rn isotopes. For Po data are taken from [Vel02, Jul01]. For Rn data are taken from [Tay99, Tay96, Fre94, Hor81].

In the radon isotopes, ^{202}Rn is predicted to be the lightest nearly spherical isotope with quadrupole deformation of $\beta_2 = -0.10$ before the change in ground-state deformation takes place in ^{201}Rn with $\beta_2 = -0.20$ [Möl95, Ben84]. Experimentally this change in the quadrupole deformation has been investigated in even-even radon isotopes down to ^{198}Rn through in-beam gamma-ray spectroscopic measurements [Tay99, Tay96, Fre94, Hor81]. Although a slight steepening in the decrease of the excitation energy of the 2^+ state was observed starting from ^{200}Rn (see figure 2.6), no result consistent with the theoretical predictions of a sizeable ground-state deformation was discovered even in ^{198}Rn [Tay99]. On the other hand, the fall of the excitation energies of higher spin states (4^+ and 6^+) with decreasing neutron number in isotopes with $A \leq 200$ may indicate that the spherical structures are there crossed by structures similar to the oblate intruder states in Po isotopes [Dob02].

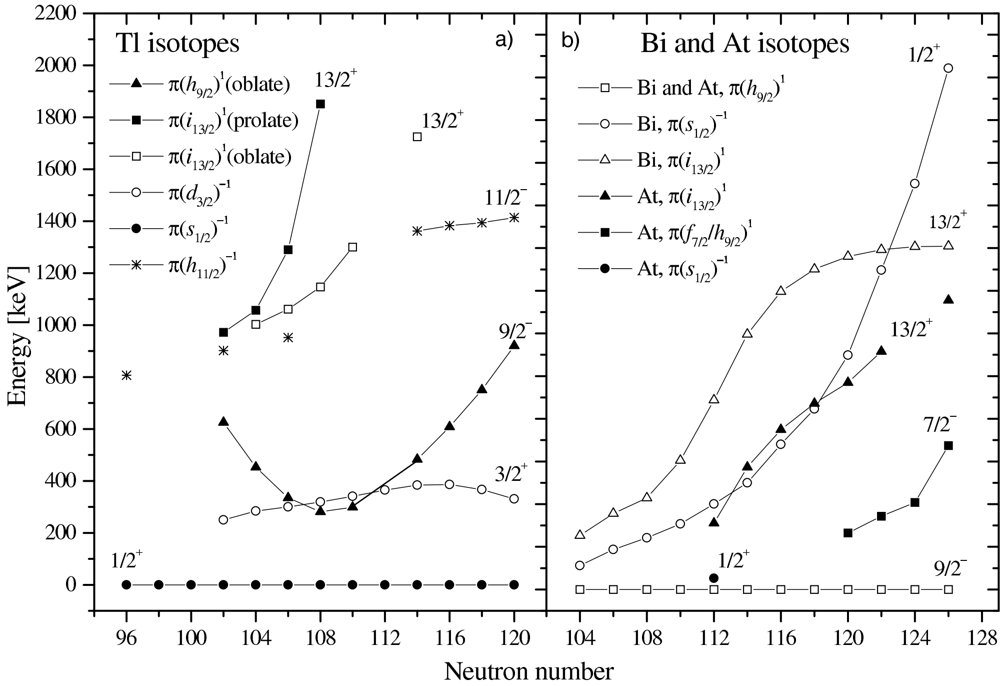

Figure 2.7: a) Level systematics for odd-mass Tl isotopes taken from [Mui01]. b) Level systematics for odd-mass Bi and At isotopes. Data taken for Bi from [Bat99, Hür02, Wau97, And01, Coe85, Nie01, Fir96] and for At from [Coe86, Smi99, Lac00, Dyb83, Fir96].

The studies of odd-Z nuclei provide an important possibility to gain information on the ordering and the energy of single-proton levels. The level systematics of odd-mass thallium isotopes, with $Z = 81$, is shown in figure 2.7 a). For these nuclei a nearly spherical $1/2^+$ state is observed to be the ground state [Hey83, Coe85], which is concluded to originate from a proton-hole in the $s_{1/2}$ orbital. In the mid-shell region a low-lying $9/2^-$ state has been identified via alpha-decay measurements. This intruder state is deduced to originate from a proton excitation across the $Z = 82$ shell gap to the $\pi h_{9/2}$ orbital and is associated with an oblate-deformed $\pi(1p - 2h)$ configuration. In the Nilsson diagram this state is associated with the $9/2^-[505]$ orbital. The excitation energy systematics of the state exhibit a parabolic behaviour as a function of neutron number, with the minimum at $N = 108$ close to the neutron mid-shell [Hey83, Coe85]. In addition, the systematics of the $i_{13/2}$ proton-particle states and the $d_{3/2}$ and $h_{11/2}$ proton-hole states are shown in figure 2.7 a). In the gold isotopes with $Z = 79$, only three protons below the lead core, the down sloping behaviour of the states is even steeper. The nearly spherical structures are crossed by the deformed structures in the mid-shell region causing a change in the ground state assignment [Hey83].

The bismuth isotopes, with $Z = 83$, have one extra proton compared to the proton-magic lead. Thus, the ordering of the $1/2^+$ and the $9/2^-$ states is inverted compared to the thallium isotopes, as shown in figure 2.7 b). In the bismuth isotopes the $9/2^-$ state, associated with a proton in the $h_{9/2}$ orbital, is identified as the ground state. The steeply sloping $1/2^+$ intruder state with a $\pi(2p - 1h)$ configuration is concluded to originate from the excitation of an $s_{1/2}$ proton across the $Z = 82$ shell gap to the $\pi h_{9/2}$ orbital. The $1/2^+$ state exhibits a parabolic energy dependence on the neutron number in the same way as the $9/2^-$ state in the thallium isotopes. However, the excitation energy of the $1/2^+$ state is observed to still decrease at the mid-shell nucleus $^{187}\text{Bi}_{104}$ [Bat99]. It is speculated that the continuing downward trend could arise from a crossing of two different $1/2^+$ states. A weakly oblate-deformed configuration would create the parabolic behaviour in the heavier odd-mass bismuth isotopes. In the lighter isotopes, a prolate $1/2^+$ state would cross the oblate state and continue the downward trend of the $1/2^+$ state. Recent theoretical calculations [And03] agree with the idea of a crossing of the oblate and prolate state and suggest the $1/2^+[400]$ orbital for the prolate configuration. The systematics of the bismuth isotopes can be compared to the crossing of the different shapes in lead and polonium isotopes (figures 2.5 and 2.6).

In the astatine isotopes, with $Z = 85$, an even more dramatic sloping of the states can be expected, similar to that in the gold isotopes. Hints of this kind of behaviour can be seen in the level systematics shown in figure 2.7b). The first identification of a $1/2^+$ intruder state in the astatine isotopes (associated with an oblate $\pi(4p - 1h)$ configuration) was reported by Coenen *et al.* [Coe86] in ^{197}At. The low excitation energy (52(10) keV) of this state in ^{197}At led them to the conclusion that the $1/2^+$ state may become the ground state in ^{195}At. In addition, the ground state quadrupole deformation of astatine isotopes is theoretically predicted to change from $\beta_2 = 0.08$ to $\beta_2 = -0.21$ between ^{199}At and ^{198}At by Möller *et al.* [Möl95]. In contradiction to the theoretical calculations, in-beam gamma-ray spectroscopic measurements of odd-mass isotopes from ^{209}At to ^{197}At [Sjo76, Sjo81, Sjo82, Dyb83, Lac00, Smi99] do not show clear evidence for ground-state deformation in the neutron-deficient astatine isotopes. However, the steep decrease of the excitation energy of the $13/2^+$ state in ^{199}At and ^{197}At could be interpreted as an indication of increasing collectivity, at least in this particular state.

3 Experimental methods

The synthesis of the neutron deficient nuclei discussed in the present work is based on heavy-ion induced fusion-evaporation reactions. Iron beams (^{54}Fe and ^{56}Fe) needed for the bombardment of ^{141}Pr target nuclei were produced by using the volatile compounds (MIVOC) [Koi94] method in the ECR [Ärj90, Koi01] ion source. A ^{78}Kr beam used for the bombardment of ^{96}Ru and ^{102}Pd targets was produced from enriched krypton gas. Low-energy ion beams obtained from the ECR ion source were accelerated to the kinetic energy of approximately 5 MeV/nucleon and delivered to the target by the $K = 130$ MeV cyclotron [Liu92, Hei95] of the Accelerator Laboratory at the Department of Physics of the University of Jyväskylä (JYFL).

The variety of the different reaction channels in the heavy ion collisions used in the present work is large. Only a small part of the collisions end up in the products of interest. For the spectroscopic measurements, the desired products have to be separated and identified from the enormous background of the other reaction channels. In the present work the fusion-evaporation residues were separated in-flight from primary-beam particles and other products recoiling out from the target using the JYFL gas-filled recoil separator RITU [Lei95a]. After separation, the fusion products were focused and implanted into a position sensitive silicon detector which is the main component in the focal plane detector system. The final identification of the implanted fusion-evaporation residues is based on the method of position and time correlation [Sch84, Sch00] with the subsequent proton and alpha decays being identified in the silicon detector.

3.1 Heavy-ion induced fusion-evaporation reactions

The use of a heavy-ion induced fusion-evaporation reaction is the basic method when studying neutron deficient nuclei. The Coulomb repulsion bends the line of stable nuclei off from the $N = Z$ line to the neutron rich side. This offers the possibility to access the side of neutron deficient nuclei just by the fusing of two stable nuclei as illustrated in figure 3.1.

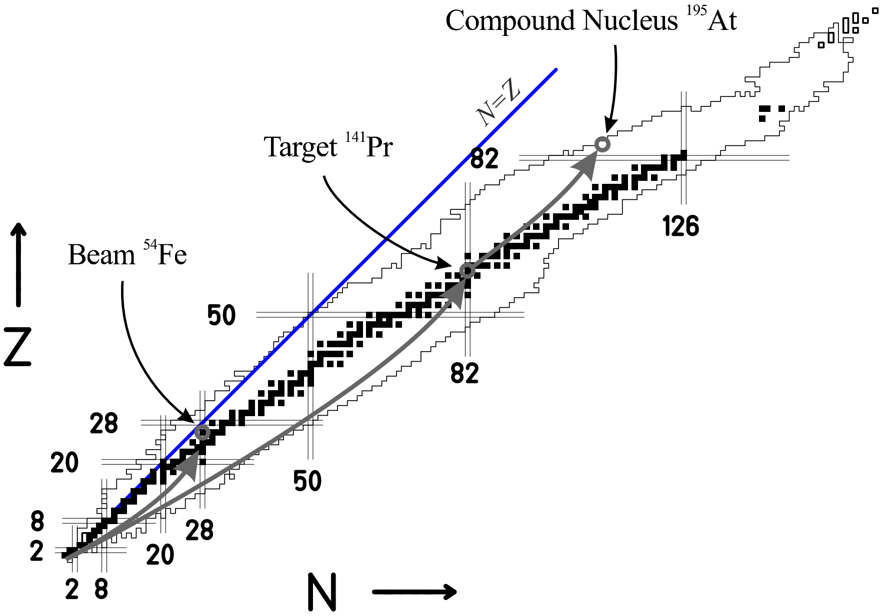

Figure 3.1: View of the nuclear chart showing how the fusion reaction of two stable nuclei can be used to probe the neutron deficient nuclei beyond the proton drip line.

In order to fuse the projectile and target nuclei, the kinetic energy of the projectile particle has to overcome the repulsive fusion barrier which is mainly caused by the Coulomb force between the nuclei. If the energy of the projectile is less than the height of the barrier it has to penetrate through the energy barrier, but this decreases dramatically the probability of the fusion reaction. The height of the fusion barrier can be roughly estimated using the height of the Coulomb barrier B_{Coul} at the point where the projectile and the target nucleus touch each other. Assuming spherical nuclei the height of the barrier can be estimated by the equation

$$B_{Coul} \approx \frac{Z_p Z_t}{A_p^{1/3} + A_t^{1/3}} \quad \text{[MeV]} \tag{3.1}$$

where Z_p, A_p, Z_t and A_t are the proton and mass numbers of the projectile and target nuclei, respectively. For more accurate calculations the Bass barrier [Bas80] is often used in the heavy element region. This formula takes into account also the effect of the nuclear potentials and angular momentum between the colliding nuclei.

After the fusion process, the compound nucleus is in an excited state. The excitation energy E^* can be calculated by summing the kinetic energy of the nuclei E_{cm} in the center of mass system with the reaction Q-value. In a more practical form, the center of mass energy E_{cm} can be expressed by the kinetic energy of the projectile nucleus in laboratory coordinates E_{lab} using the mass numbers of the target and projectile nuclei. Correspondingly, the reaction Q-value can be calculated using the atomic masses. Thus the excitation energy of the compound nucleus is

$$E^* = E_{cm} + Q \approx \frac{A_t}{A_p + A_t} E_{lab} + (M_p + M_t - M_{cn})c^2 \tag{3.2}$$

where M_p, M_t and M_{cn} are the atomic masses of the projectile, the target and the compound nucleus, respectively.

In fusion reactions, where the kinetic energy of the projectile is greater than the fusion barrier energy, the excitation energy and also the angular momentum of the compound nucleus can be high (even more than 100 MeV and 100 $\hbar$). In the present work the excitation energies of the compound nuclei were in the range of $35 - 60$ MeV. The de-excitation of a highly excited compound nucleus is a complicated process and may go through several various decay channels like fission or a cascade of particle evaporations. In the present work the nuclei of interest were produced via de-excitation channels where neutrons or protons were evaporated. For example, ^{170}Au was produced via evaporation of one proton and three neutrons (p3n-channel) from the compound nucleus ^{174}Hg. One evaporated neutron lowers the excitation energy of the nucleus by approximately 8 to 15 MeV depending on the excitation energy and the region of the nuclear chart in question. This information can be used to estimate the excitation energy needed for the evaporation of a certain number of particles. In the fusion evaporation reactions used in the present work (4n, p2n and p3n) one evaporated particle reduces the excitation energy of the nucleus approximately 15 MeV.

The probability that the evaporation process ends up in a particular final product is described by the production cross section σ. If the total production rate of a certain evaporation residue is R, when a target with N target nuclei per unit area is bombarded by the projectile beam with intensity I, the cross section for the production of these residues is

$$\sigma = \frac{R}{N \cdot I} \tag{3.3}$$

Usually, it is not possible to observe all the evaporation residues of interest using experimental devices. Thus, the number of observed events has to be corrected with the efficiency of the experimental set-up for the estimation of the production cross section. In the present work the quantities used for this correction are 40 % for the efficiency of the separator and 55 % for the probability that a proton or an alpha particle originating from the decay of a nucleus in the silicon detector deposits all its kinetic energy into the detector.

Around mass region $A \sim 200$ and close to stability, the evaporation of neutrons dominates if the excitation energy and the angular momentum of the compound nucleus are moderate. This is due to the Coulomb barrier which hinders the evaporation of charged particles. In lighter nuclei where the Coulomb barrier is lower, the probability for the evaporation of charged particles increases. Correspondingly, in heavier nuclei the evaporation of alpha particles is more favoured due to the increase in the alpha emission Q-values. In addition, fission competition becomes important in heavier nuclei due to the lowering of the fission barrier (fissility $\propto Z^2/A$).

When approaching the proton drip line those reaction channels which involve the evaporation of charged particles become more dominating due to changes in proton, neutron and alpha particle separation energies. Above $Z = 82$ fissility increases quickly with Z, and xn-channels are usually the best choices even at the edge of the known nuclei. Nevertheless, the cross sections of xn-channels decrease quite rapidly due to the fission competition when moving to the more neutron deficient nuclei. An illustrative example is given by the cross sections of 300 pb and 40 nb measured for ^{191}At and ^{193}At, respectively, when utilising the 4n-channel.

Below $Z = 82$ fissility is moderate even beyond the proton drip line. In the proton unbound nuclei the pure xn-channels are hindered since the proton evaporation is dominating. But due to the variation in the position of the proton drip line between the odd-Z and the even-Z nuclei (see figure 1.1) the pxn-channels can be used to probe nuclei far beyond the drip line, in the region of proton emitting nuclei. In pxn-channels the evaporation process can be thought to proceed first via neutron evaporation along the isotopes of even-Z nuclei where protons are still bound and therefore not evaporated as easily as in the odd-Z nuclei below. Finally, after neutron evaporation the reaction channel ends up in the proton radioactive nucleus far beyond the proton drip line via evaporation of one proton. The evaporation of as many as five neutrons in the pxn-channel (p5n) was successfully used to identify the proton radioactivities ^{140}Ho [Ryk99], ^{164}Ir [Ket01a, Mah02] and ^{130}Eu [Mah02].

Since fission competes with particle evaporation at each step of the evaporation cascade (especially in heavy nuclei), it is better to select the projectile-target combination in such a way that the compound nucleus is close to the evaporation product of interest. Thus, long evaporation chains are avoided and the survival of the residue is more probable. However, when the bombarding energy of the beam particles exceeds the fusion barrier, the excitation energy of the compound nucleus is so high that at least one to three particles will be in any case evaporated. For example, in the present work, the cross sections for the evaporation of only two particles in the $^{54,56}\mathrm{Fe} + {}^{141}\mathrm{Pr}$ reactions are lowered since the optimum bombarding energy does not overcome the fusion barrier. In addition, certain practical limitations like availability of targets and ion beams have an effect on the selection of the projectile-target combination.

3.2 Recoil separators

In order to study the spectroscopic properties of the nuclei of interest they have to be separated from the primary heavy-ion beam particles and the other reaction products. Nowadays recoil separators can be considered as the primary tool in the studies of neutron deficient heavy nuclei. The working principle of separators is based on the capability of magnetic and electric fields to separate particles having different mass to charge ratios or velocities to different spatial trajectories.

In a magnetic field the track of a charged particle is defined by the Lorentz force. If a particle with electric charge q and mass m moves in a homogeneous magnetic field B with velocity v perpendicular to the field the magnetic rigidity $B\rho$ of the particle is defined by the equation

$$B\rho = \frac{mv}{q} \quad [\mathrm{Tm}] \tag{3.4}$$

where ρ describes the radius of the particle track in the magnetic field.

When the fusion products recoil out from the target their charge and velocity distributions are broad. In vacuum mode mass separators where the charge states are not affected after the target or a possible reset foil, the spatial distribution of the recoils after the dipole magnet is very wide according to equation 3.4. Thus, it is not possible to guide the recoils of interest through the separator and focus them to a detector system at the focal plane without significant losses (see figure 3.2). Although only a couple of charge states can be focused to the detector a great advantage of vacuum mode mass separators is high mass resolving power, which can be the most significant property for some experiments.

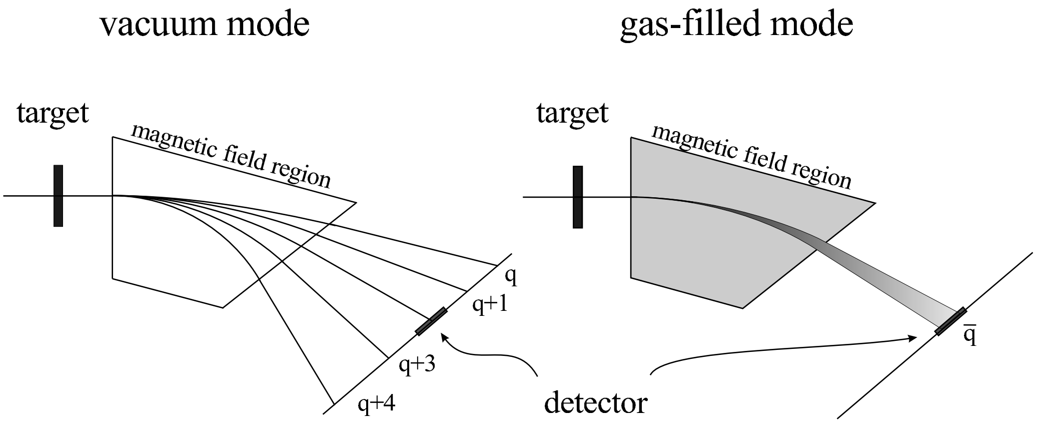

Figure 3.2: The main principal difference between vacuum mode and gas-filled magnetic recoil separators. In vacuum the ions follow discrete trajectories defined by the charge states. In gas the charge states of the ions vary around the average charge state and the ions follow an average trajectory.

To avoid the effect of a broad charge state distribution the volume of the separator can be filled by gas. When heavy ions penetrate the gas they undergo atomic charge-changing collisions. This makes the charge state of the ions change around the mean charge state $\overline{q}$. According to Bohr theory an ion which is moving in a gas loses those electrons whose speed is less than its own speed [Ghi88]. According to the Thomas-Fermi atomic model the number of such electrons is

$$\overline{q} = \frac{v}{v_o} Z^{1/3} \tag{3.5}$$

if the velocity v of the ion is in the range

$$1 < \frac{v}{v_o} < Z^{2/3} \tag{3.6}$$

In these equations v_o is the Bohr velocity ($2.19 \cdot 10^6$ m/s) and Z is the atomic number of the ion. Replacing the nuclear mass m, velocity v and charge state q in equation 3.4 by nuclear mass number A, the ratio of the velocity and Bohr velocity v/v_o and average charge state $\overline{q}$ and using equation 3.5, one obtains the following equation for the magnetic rigidity of the ion in gas

$$B\rho \approx 0.0227 \frac{v}{v_o} \frac{1}{q} A \approx 0.0227 \frac{A}{Z^{1/3}} \quad [\text{Tm}]. \tag{3.7}$$

This first order approximation for the $B\rho$ of the ion in gas is dependent only on the mass number A and the atomic number Z of the ion and it is independent of the velocity and the original charge state of the ion. Due to this the spatial distribution of the recoils after separation is narrower and thus the recoil collection efficiency higher than in vacuum mode. The trajectories of the ions in vacuum and in a gas filled magnetic field region are outlined in figure 3.2. A disadvantage which follows from the use of the filling gas is the decrease in the mass resolving power. Typical mass resolution of gas-filled recoil separators is 10 % which is not enough to separate the products of different fusion evaporation channels. In the present work the final identification of the reaction products is based on the properties of the subsequent decay chains observed in a silicon strip detector after the implantation.

3.2.1 Gas-filled recoil separator RITU

The gas-filled recoil separator RITU (Recoil Ion Transport Unit) shown in figure 3.3 is designed for the studies of exotic super heavy elements using asymmetric fusion reactions. During the past years it has been noticed that the separator works nicely also for the studies of the neutron deficient nuclei around the lead region utilising rather symmetric fusion reactions. After the redesign of the dipole chamber and the beam stop the separator performs even better. The most important technical parameters of RITU are collected in table 3.1.

Table 3.1: Technical parameters of RITU.

Magnetic configuration	$Q_1DQ_2Q_3$	Q_1 effective length	350 mm
Maximum beam rigidity	2.2 Tm	Q_1 maximum gradient	13.5 T/m
Bending radius	1.85 m	Q_1 aperture diameter	105 mm
Acceptance (horizontal)	±30 mrad	$Q_{2,3}$ effective length	600 mm
Acceptance (vertical)	±80 mrad	$Q_{2,3}$ maximum gradient	6.0 T/m
Dispersion	10 mm/%	$Q_{2,3}$ aperture diameter	200 mm
Dipole bending angle	25°	Total weight	17500 kg
Dipole pole gap	100 mm	Total length	4.8 m

Transmission of recoils for the xn- and pxn-channels of the reactions used in the present work $\sim$ 40 %

Traditionally, gas-filled recoil separators consist of a dipole magnet for primary separation and two quadrupole magnets. This ion-optical configuration is usually expressed with letters DQQ, where D corresponds to a magnetic

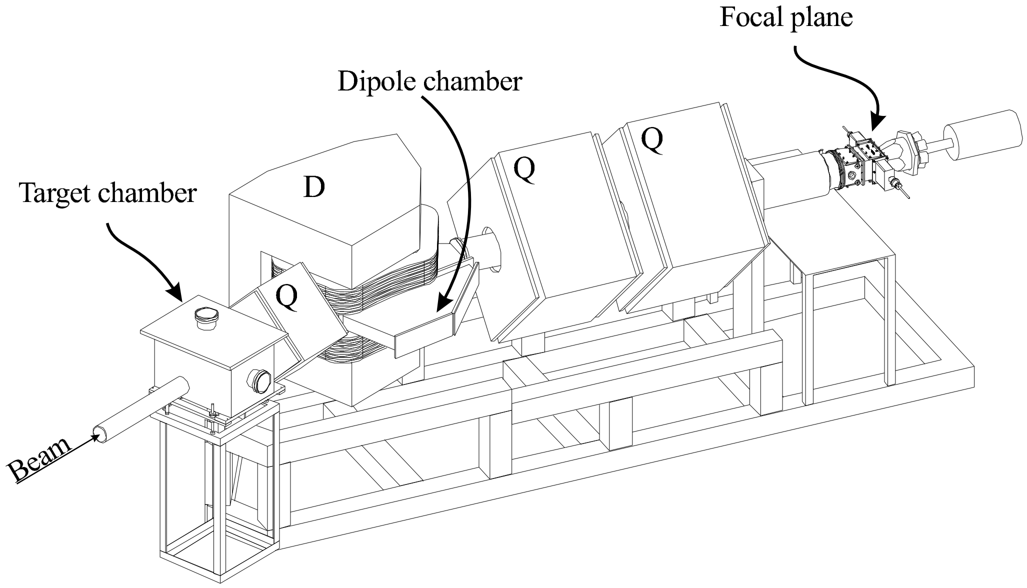

Figure 3.3: A schematic drawing of the gas-filled recoil separator RITU. A Compton-suppressed Nordball-type germanium detector is placed adjacent to the silicon detector for gamma- and X-ray detection.

dipole field and Q to a quadrupole field. In the RITU separator an extra focusing quadrupole magnet is added in front of the dipole magnet and the ion-optics represents a QDQQ configuration. The idea of an additional quadrupole magnet is to focus the reaction products in the vertical direction inside the dipole magnet and thus increase the transmission of the separator. At the same time, however, the scattering of the reaction products from the helium-filling gas increases due to the longer flight path of the fusion products in the filling gas, decreasing the transmission of the separator. The advantage of the additional quadrupole magnet has been observed in asymmetric reactions where the velocities of the fusion products are low and the angular distribution large. In symmetric reactions where the angular distribution is sharp the use of the first quadrupole magnet does not affect the transmission. In fact, it tends to increase the amount of background events at the focal plane by attempting to squeeze all the other reaction products and scattered beam particles inside the dipole magnet in the vertical direction causing the widening of the distribution in the horizontal direction. Since the reactions used in the present work were quite symmetric only a low magnetic field was used in the first quadrupole magnet to avoid collecting too many background events to the focal plane detector system.

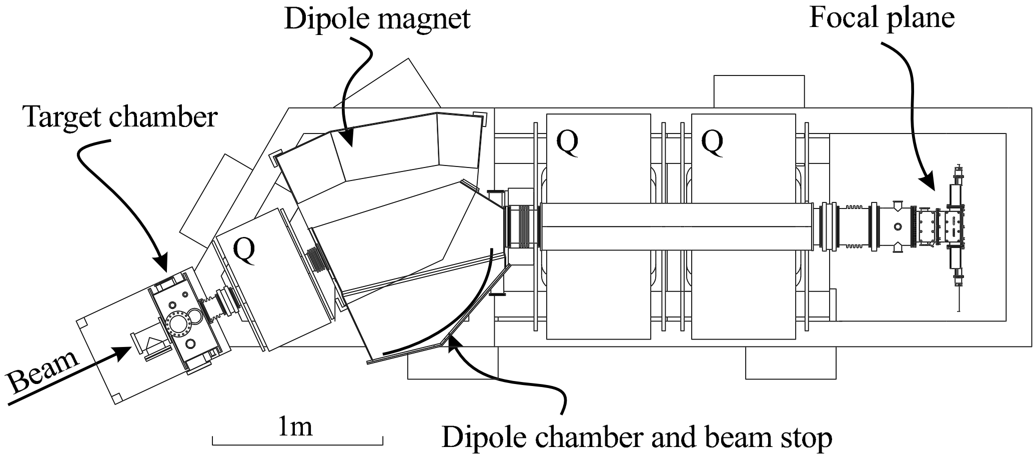

Figure 3.4: Top view showing the arrangement of the separator.

In figure 3.4 the heavy-ion beam enters the gas-filled recoil separator RITU from the left along the high vacuum beam line of the cyclotron. In measurements discussed in publications **I** and **III** the gas volume of RITU, filled with $0.5-1.5\,\mathrm{mbar}$ of helium, was separated from the cyclotron high vacuum beam line by a thin carbon foil approximately $50\,\mu\mathrm{g/cm}^2$ of thickness. For the measurements discussed in publication **II** very high beam intensities were needed and instead of using a carbon window a differential pumping system for helium filling gas was used in front of the separator. Figure 3.5 shows the schematic drawing of the differential pumping system which was based on two collimators, one Roots pump station and turbo pump stations. The inlet of helium gas was controlled using a manual needle valve. After passing the beam window or the differential pumping system the fine adjustment of the beam energy could be made using a set of thin carbon foils in front of the target. After the degraders the beam hit a thin, usually $500-1000\,\mu\mathrm{g/cm}^2$ thick target foil. In the measurements discussed in publications **I** and **III** stationary targets were used and beam intensities were limited mainly because of the endurance of the targets. For high beam intensity measurements, discussed in publication **II**, a rotating target was used. The target was rotated in the ion beam such that the rotating axis was approximately 10 mm off from the primary beam axis. This procedure allowed the use of higher ^{56}Fe and ^{54}Fe beam intensities up to 100 pnA.

Due to a thin target foil and the momentum of the beam particles the reaction products recoil out of the target and fly to forward angles (beam direction) inside the first quadrupole magnet. The dipole magnet separates the

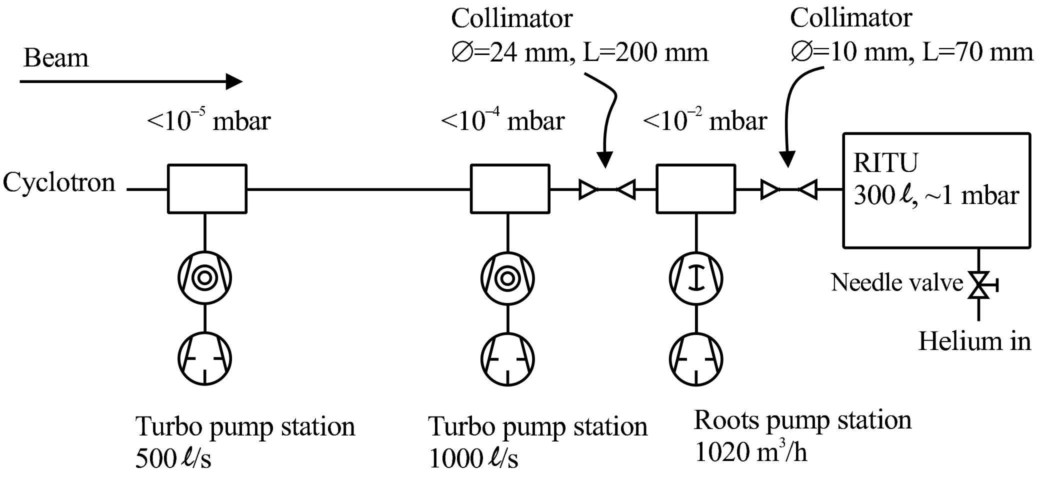

Figure 3.5: Schematic drawing outlining the differential pumping of helium filling gas of RITU.

fusion-evaporation products from the primary beam particles and the other reaction products, which are stopped on the beam stop inside the dipole chamber shown in figure 3.4. Then the fusion products are focused to the detector system at the focal plane of the separator using two quadrupole magnets. The optimum settings of the separator were established based on the online monitoring of the particle energy spectra detected at the focal plane detector system.

3.2.2 Modification of the dipole chamber of RITU

The dipole chamber and the beam stop of the gas-filled recoil separator RITU were modified in order to improve the suppression of the background events (mainly scattered beam) at the focal plane detector system. The modifications to the dipole chamber and the beam stop are illustrated in figure 3.6. In the recoil separator RITU the beam particles and fusion products are separated in gas using a magnetic dipole field. The beam particles which have smaller magnetic rigidities follow a trajectory with a much tighter radius than fusion products and are thus dumped in the beam stop inside the dipole chamber.

In the original design the beam stop was placed quite close to the optical axis of the separator and fully inside the dipole magnet. This allowed the possibility that some of the beam particles which were scattered from the beam stop were transported to the focal plane. It was also possible to improve the design of the walls of the old dipole chamber. When using symmetric

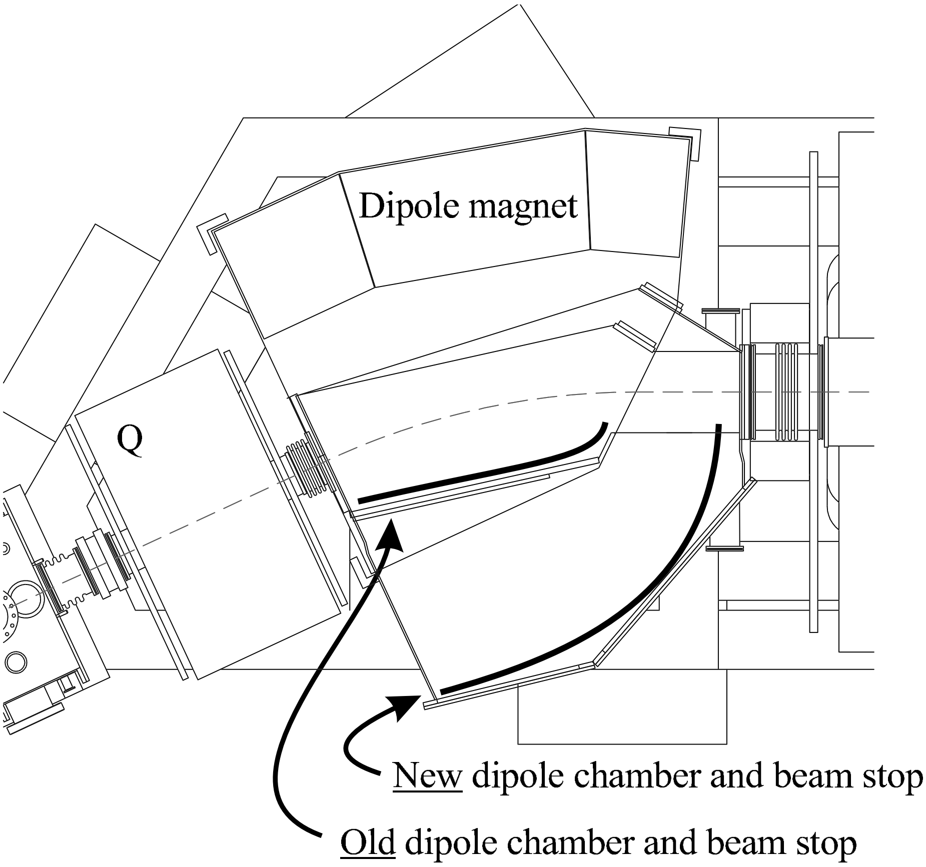

Figure 3.6: A drawing outlining the modifications to the dipole chamber and beam stop of the RITU separator. The dashed line shows the optical axis of the separator.

reactions, where the differences between the magnetic rigidities of the beam particles and fusion products are small, beam particles could pass the edge of the old beam stop and scatter from the wall behind it to the focal plane. In the new design the dipole chamber is much larger and care was taken to avoid walls which could scatter particles to the focal plane. The beam stop is placed much further away from the dipole magnet giving more time and space for the separation. This is important especially in symmetric reactions as mentioned above. Also the shape of the new beam stop is designed so that the separated particles are dumped perpendicular to the beam stop to avoid scattering of the particles back into the separator.

Figure 3.7 shows the effect of the new design on the total spectrum measured with the silicon strip detector at the focal plane. Both spectra are measured in the bombardment of a ^{109}Ag target with a ^{83}Kr beam at an energy of 357 MeV in the middle of the target. The upper panel shows the total spec-

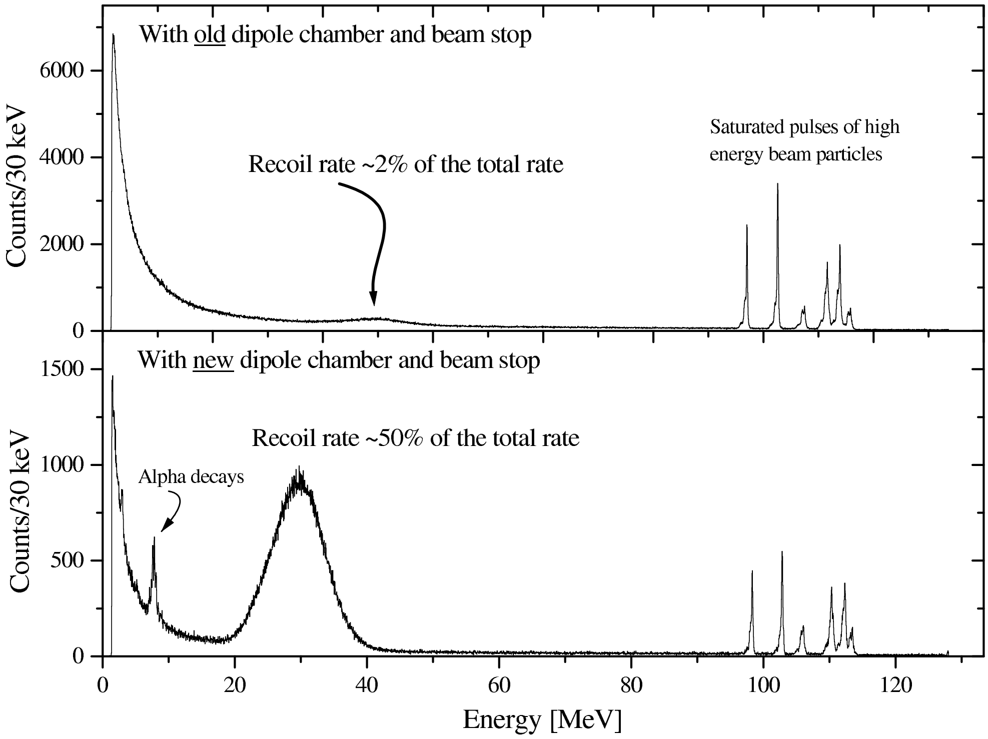

Figure 3.7: The effects of the modification of the dipole chamber and the beam stop to the energy spectra of the events observed at the focal plane silicon detector in ^{83}Kr + ^{109}Ag reaction. The upper spectrum is measured with the original design and the lower with the modified dipole chamber and beam stop.

trum measured with the original dipole chamber. The counting rate of the fusion products was approximately 2 % of the total counting rate and their contribution is hardly visible in the spectrum. The lower panel in figure 3.7 shows the total spectrum from the same reaction but now measured after the installation of the new dipole chamber and the beam stop. For this reaction the background is reduced by a factor of 25 and the counting rate of fusion products was approximately 50 % of the total rate. Fusion products and even alpha-decay peaks are clearly visible in the spectrum measured after modification.

3.3 Focal plane set-up

Separated fusion-evaporation residues were focused and implanted into a boron implanted position-sensitive (PIPS Passivated Implanted Planar Silicon) silicon strip detector at the focal-plane detector system shown in figure 3.8. The final identification of the implanted products was based on the method of position and time correlation [Sch84, Sch00] with the subsequent decays in the silicon strip detector. Two gas counters were installed upstream from the silicon detector for the detection of passing-through particles. Behind the silicon strip detector two quadrant silicon detectors were installed for the detection of light and energetic punch-through particles and beta particles. Just in front of the silicon strip detector a set of degrader foils, made of Mylar, were installed affording a possibility to select (decrease) the implantation energy of recoils and to stop low energy scattered beam particles. For gamma- and X-ray detection at the focal plane a Compton-suppressed Nordball-type germanium detector [Mos89] with a relative efficiency of 40 % was placed adjacent to the silicon detector.

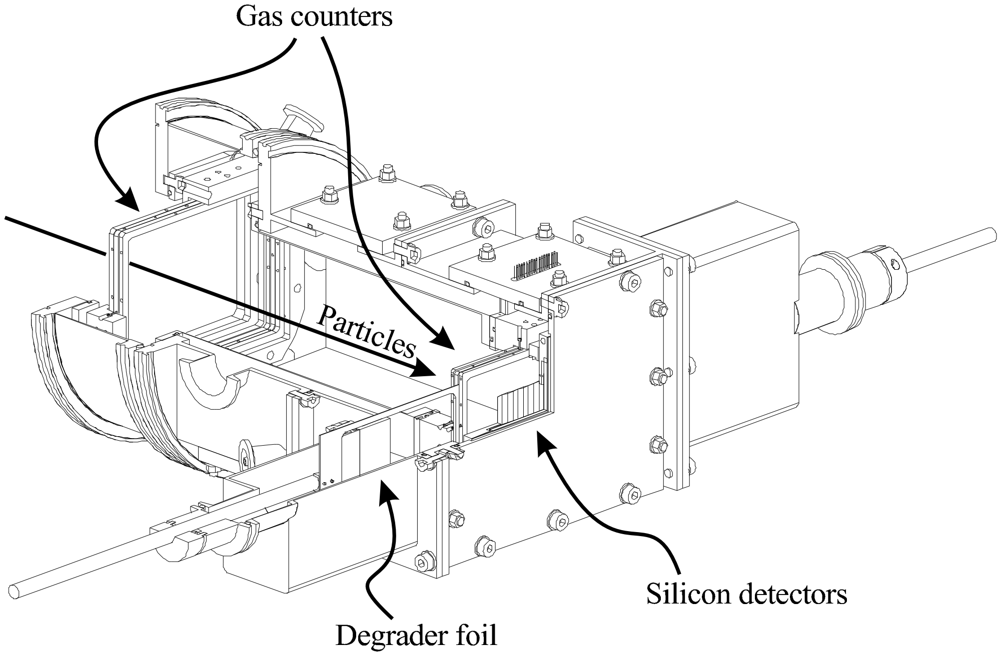

Figure 3.8: The focal-plane detector system used in the experiments of the present work. The arrangement of the germanium detector used for gamma- and X-ray detection is shown in figure 3.3 and discussed later in section 3.3.4.

The signals from the detectors were processed with standard NIM electronics. The amplified signals were digitised in NIM and CAMAC based analogue-to-digital converters (ADC) and fed into the data acquisition system. The data acquisition system was based on a set of VME crates with integrated electronics and a control workstation [Jon95]. The read-out controller read out the ADC cards information only when a master trigger signal (event in the silicon strip detector) was present. The events were stored in a high-speed memory and when the memory was filled the data blocks were read out and converted into Eurogam format [Cre91]. The data blocks were sent to a tape server and written onto magnetic Exabyte tape. The data acquisition system was controlled by the MIDAS data acquisition control running on a SUN workstation. The workstation allowed the on-line sorting of the data written onto tape. Thus a number of various spectra were created for on-line monitoring of the experiment. The progress of the experiment was also confirmed by searching for correlated decay chains on-line.

3.3.1 Silicon strip detector for spectroscopic measurements

A position sensitive silicon strip detector was used for the spectroscopic measurements. The detector of thickness $305\,\mu$m and of area $80{\times}35\,\mathrm{mm}^2$ was horizontally divided into 16, 5 mm wide position-sensitive strips. Figure 3.9 shows a block diagram of the electronics components used for one individual strip. Both ends (top and bottom) of each strip were connected to a charge sensitive preamplifiers which were also used to feed an individual bias voltage to the strip typically set to -60 V. The total energy signal of the event in the strip was obtained by summing the top and bottom signals. The amplitudes of the top and bottom signals were proportional to the vertical position of the event in the strip. For the elimination of their energy dependence the raw position signals were divided by the total energy information. The normalised top and bottom positions were used for the vertical position information of the event in the strip. The vertical position resolution (full width of the position window) was typically better than $500\,\mu$m for the implantations of fusion evaporation residues and alpha decays and approximately $1000\,\mu$m for proton emission. Assuming a position resolution of $500\,\mu$m the nominal number of the detector elements in the silicon detector is on the order of 1000. However, due to the inhomogeneous distribution of recoils over the silicon detector shown in figure 3.10 the effective number of detector elements was typically reduced and was on the order of 200.

Since the energy range of the events in the silicon detector can vary from approximately one MeV for the proton emission up to more than a hundred MeV for the implantation of the fusion products, two sets of amplification channels with different gains were used. The channels with a low amplification were dedicated to the implantation events covering the energy range from approximately 5 MeV up to 150 MeV. Correspondingly, the channels with a high amplification were used for decay events covering the energy range from 600 keV up to 12 MeV. The energy resolution of the silicon strip detector in the spectrum sum of all 16 strips was typically 25 keV for 7000 keV alpha

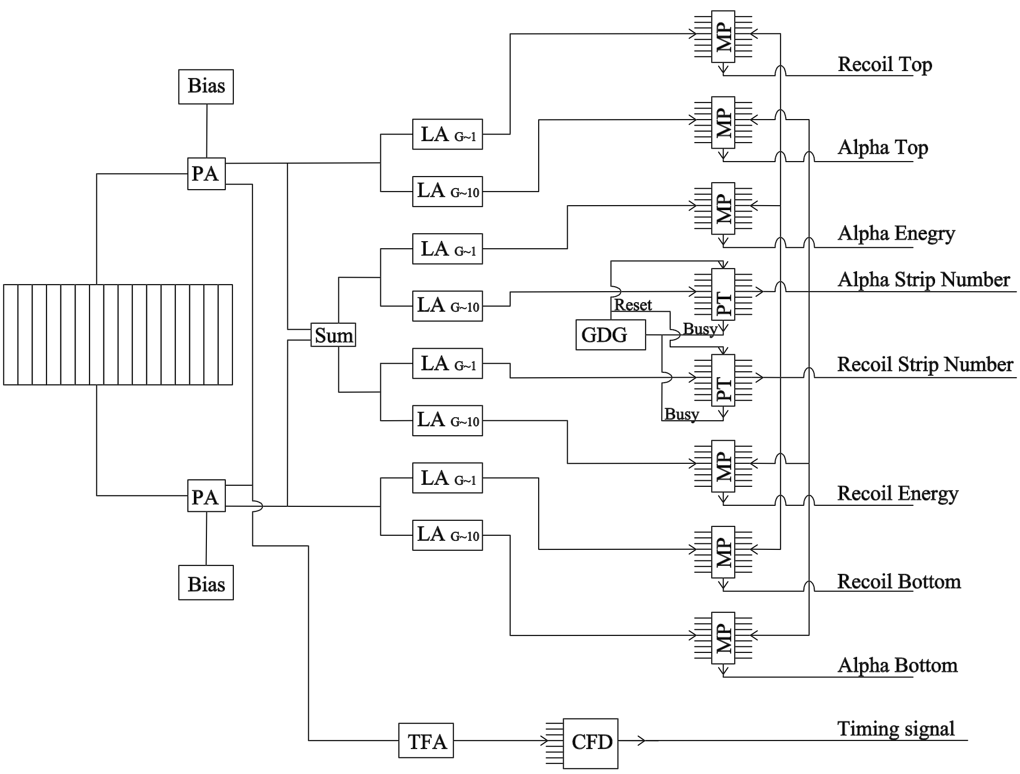

Figure 3.9: A block diagram of electronics used for one individual strip of the silicon strip detector. (PA = PreAmplifier, LA = Linear Amplifier, PT = Pattern Trigger, MP = MultiPlexer, GDG = Gate and Delay Generator, TFA = Timing Filter Amplifier, CFD = Constant Fraction Discriminator).

decay and 20 keV for 1700 keV proton emission. To minimize the effects of the radiation damages and to improve the energy and the position resolution the silicon detectors (strip and punch through detectors) were cooled down to −20 °C using circulating coolant.

Almost one hundred (6×16) amplifier channels were needed for the energy and top and bottom position information of the event in the silicon strip detector because two different amplifications were used. In addition, two more sets of sixteen channels (high and low) were needed to create the strip number (horizontal position) of the event using pattern trigger units. To avoid a large number of expensive ADC channels multiplexer units were used after the linear amplifier to select the pulses to be sent to the ADCs. The amplified signals of the same type were put into a multiplexer unit and were gated by the strip number information from pattern trigger units. The input signals corresponding to the strip number gate were sent to the ADCs

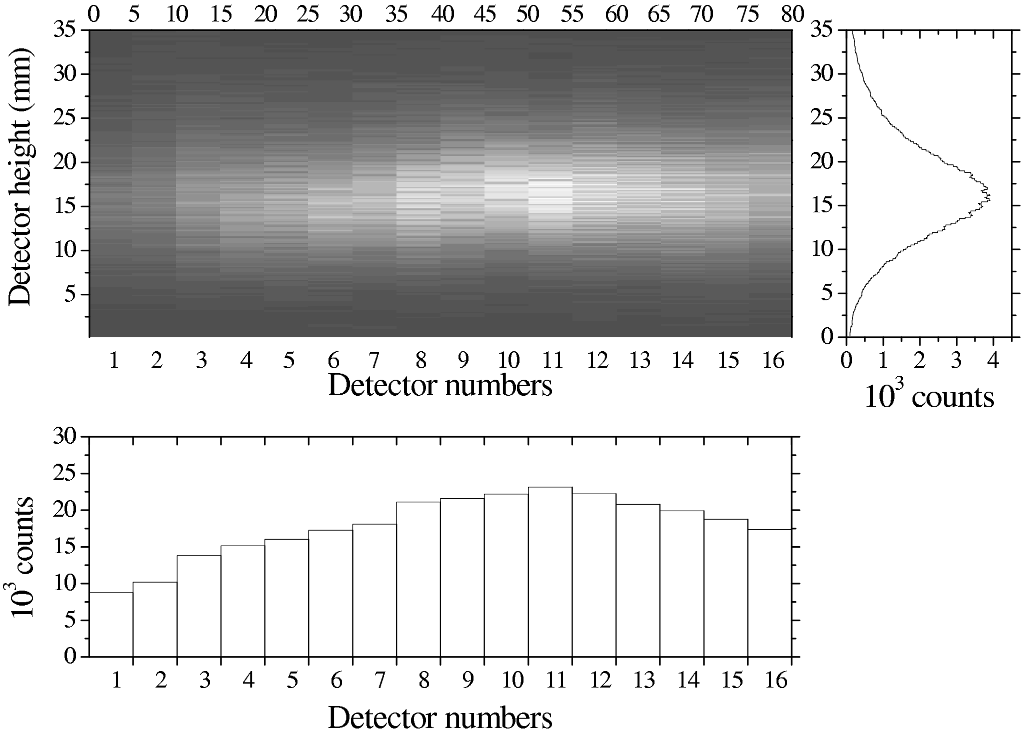

Figure 3.10: Typical recoil distribution in the silicon strip detector.

and the possible signals in the other channels were inhibited. The pattern trigger channels were also used to set the energy threshold for the signals to be collected. In all, eight linear amplification channels were needed for one individual detector strip.

3.3.2 Gas counters

Before implantation the particles pass through two multiwire proportional avalanche counters in front of the silicon strip detector. The gas counters were situated in a common gas volume filled with 3 mbar of isobutane and separated from the separator gas volume and the silicon detectors' high vacuum by $120\,\mu\text{g/cm}^2$ thick Mylar foils. The handling of the circulating gas of the counters was performed using two manual needle valves for isobutane inlet and pumping and a capacitive pressure meter to monitor the gas pressure. The first gas counter with an active area of 145 mm height and 108 mm width was placed 330 mm upstream from the silicon strip detector. The second counter with an active area of 64 mm by 108 mm was placed only 15 mm upstream from the silicon detector. Both counters consist of three planes (cathode, anode and cathode) made of gold plated tungsten wires

20 μm in diameter. In the planes, the wires were separated by 1 mm from each other and the planes were separated by 5 mm and 4 mm in the larger and the smaller gas counter, respectively. The anode voltage was typically set to +450 V so that the avalanche amplification of the electrons around the wires stayed in the proportional region. Since the counters were situated in a common gas volume, electrons were liberated to the isobutane filling gas along the whole flight path of the ions also in between the gas counters. To avoid too long drifting times of electrons and to keep the timing characteristics of the gas counters fast enough, the collection of the electrons should happen only from the narrow volume between the cathodes of the counters. To obstruct the collection of the electrons from the area behind the cathodes, voltages of typically −40 V were supplied to the cathode electrodes. Figure 3.11 shows a block diagram of the electronic components used for the gas counters. Typically an efficiency higher than 99.5 % was reached in both gas counters for the detection of passing-through particles with $A \geqslant 4$.

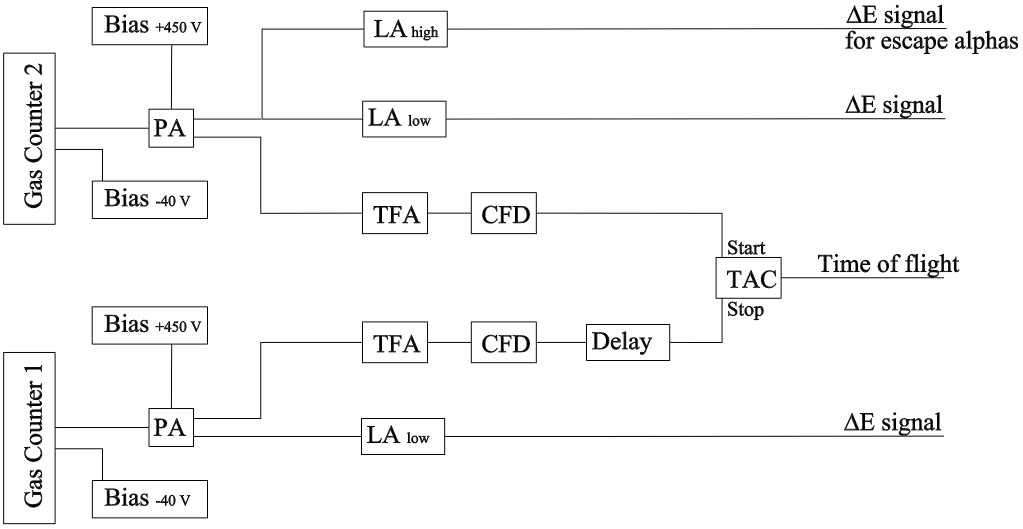

Figure 3.11: A block diagram of the electronics used for the gas counters. For the second gas counter (close to the silicon strip detector) two different amplification channels were used. One was used for the detection of heavy particles and another for the detection of escape alpha particles.

The gas counters were used to provide the energy-loss and the time-of-flight signals of the implanted particles. By combining the time-of-flight signal with the implantation energy of the particle in the silicon strip detector it was possible to easily distinguished the fusion products from scattered beam particles and transfer products, as shown in figure 3.12. This possibility to

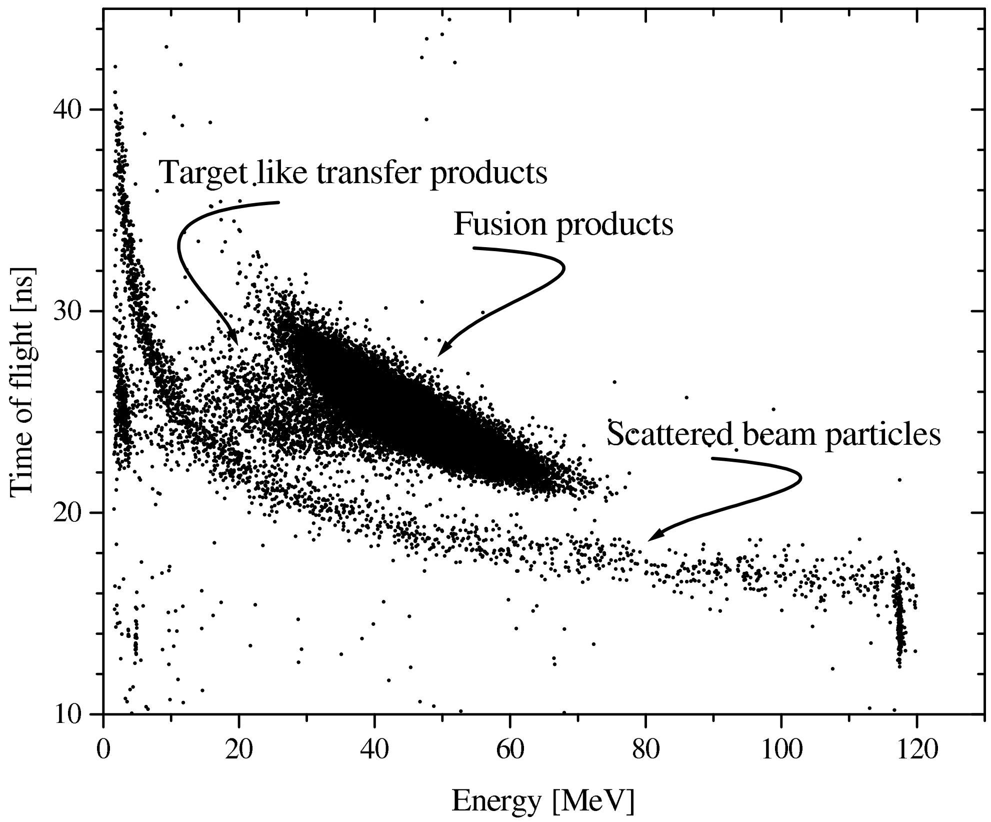

Figure 3.12: A two-dimensional time-of-flight versus energy plot for the particles implanted into the silicon strip detector. Fusion products can be easily distinguished from scattered beam particles and transfer products.

select the candidate fusion evaporation products cleans the recoil spectrum and reduces the number of accidental correlations between recoils and subsequent decay events.

The decay events in the silicon strip detector were distinguished from implantation events by demanding that the signals in the silicon strip detector were in anti-coincidence with the signals in the gas counters. This allows the collection of clean decay events (see figure 3.13). In particular, for the studies of proton emitting nuclei the second gas counter was placed only 15 mm upstream from the silicon strip detector such that it could be used to detect and veto so-called escape alpha particles. Due to the low energy loss of the light particles in the gas counter compared to heavy ions two different amplification channels were used in the second gas counter (see figure 3.11). The arrangement of the detectors is shown in figure 3.14. The typical implantation depth of the recoils in the silicon detector is only $2 - 7\,\mu$m, depending on the recoil velocity. Correspondingly, the range of a 6 MeV alpha particle in silicon is of the order of $30\,\mu$m. Thus, alpha particles emitted to backward angles can easily escape from the silicon detector such that only part of their kinetic energy is deposited into the detector. A typical energy spectrum of escape alpha particles in the strip detector and observed in the gas counter is shown as the filled spectrum in figure 3.13b). In the proton spectroscopic measurements discussed in publication **III** approximately 70 % of the escape alpha particle energies in the silicon strip detector were in the region of $1 - 2$ MeV (compare to figure 3.13b)). Unfortunately, this energy region corresponds to the typical proton emission energy. Thus the suppression of the escape alpha particles significantly increases the sensitivity of the detector systems for the observation of proton-emitting nuclei. Figure 3.13 shows a typical decay spectrum observed in the silicon strip detector after various suppression combinations.

3.3.3 Detectors for punch through particles

Behind the silicon strip detector two quadrant silicon detectors of thickness $450\,\mu$m and of area $60 \times 60\,\mathrm{mm}^2$ were installed (see figure 3.14). These detectors were mainly used to detect and veto the energetic light particles which were able to punch through the silicon strip detector. Due to the low stopping power of these particles, the gas counters were not very sensitive to them (especially to protons) and therefore the punch through particle detectors were needed. By combining the energy loss signals in the silicon detectors, the punch through particles were identified to be protons and alpha particles. The identification was based on the simulations performed using the known stopping powers of protons and alpha particles in silicon [Zie99]. A two-dimensional energy loss plot of the particles with simulated curves is shown in the upper panel in figure 3.15. The points of the minimum energy losses in the silicon detectors were used in the estimations of the maximum kinetic energies of the punch through particles. The maximum energies of approximately 20 MeV and 80 MeV were obtained for protons and alpha particles, respectively. This indicates the particles were originated from elastic head-to-head collisions with full-energy beam particles, most likely from foils at target area . The lower panel in figure 3.15 shows the energy loss spectrum of these particles in the silicon strip detector which was used for spectroscopic measurements. As can be seen the energy losses correspond to the energy regions where the proton and alpha decay peaks are expected to appear. Therefore the suppression of these events is important for proton emission as well as for alpha-decay spectroscopic measurements.

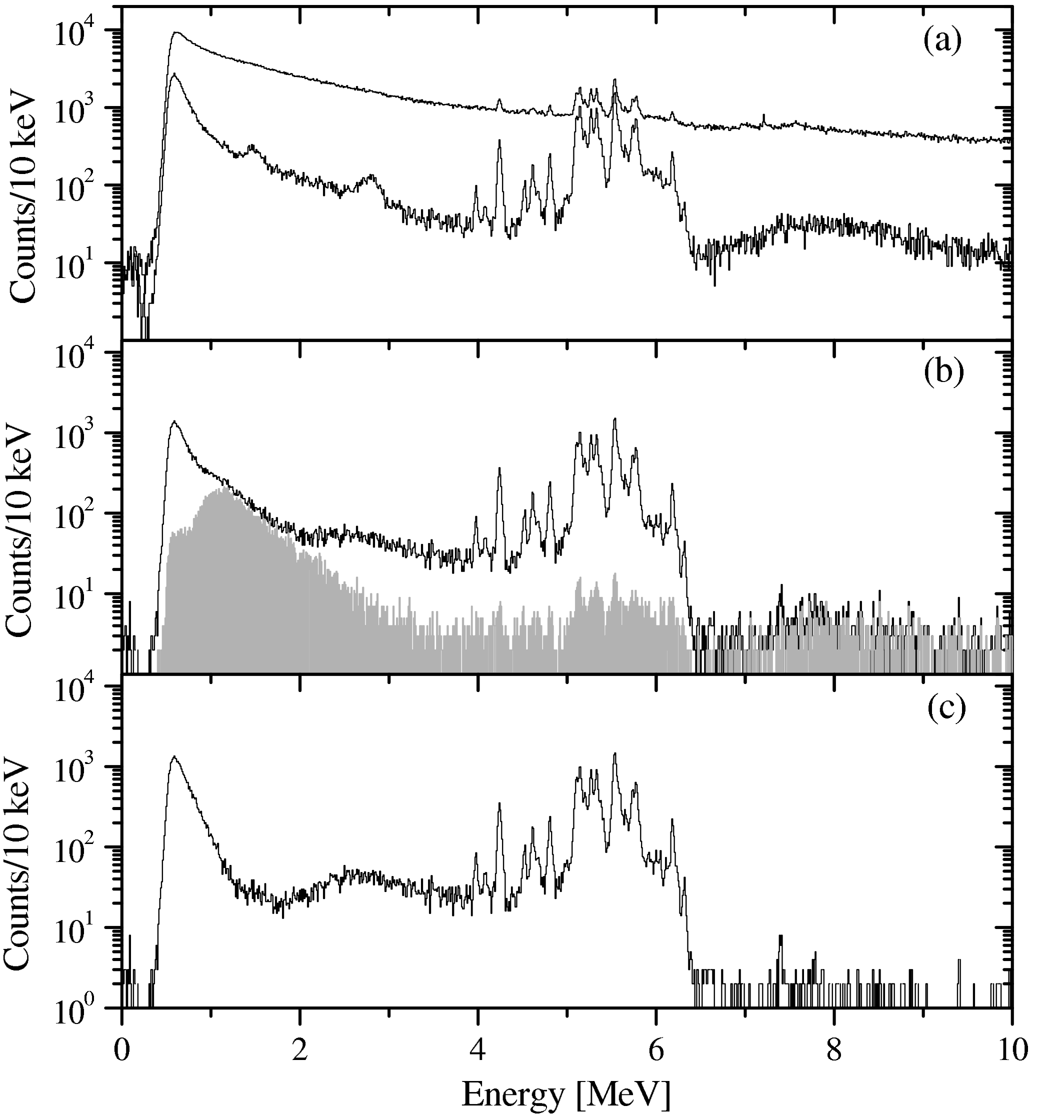

Figure 3.13: The decay energy spectra observed in the silicon strip detector after various suppression combinations in the ^{64}Zn + ^{106}Cd reaction. (a) Total and beam particle suppressed decay energy spectrum vetoed using the low gain signals of the gas counters. (b) After adding the punch through particle suppression. The filled area shows the energy spectrum of the escape-alpha particles ($E \lesssim 6$ MeV) and scattered low energy particles ($E \gtrsim 6$ MeV) detected in coincidence with the high gain signal from the second gas counter. (c) The cleaned decay spectrum observed in anti-coincidence with the gas counters and the punch through particle detector.

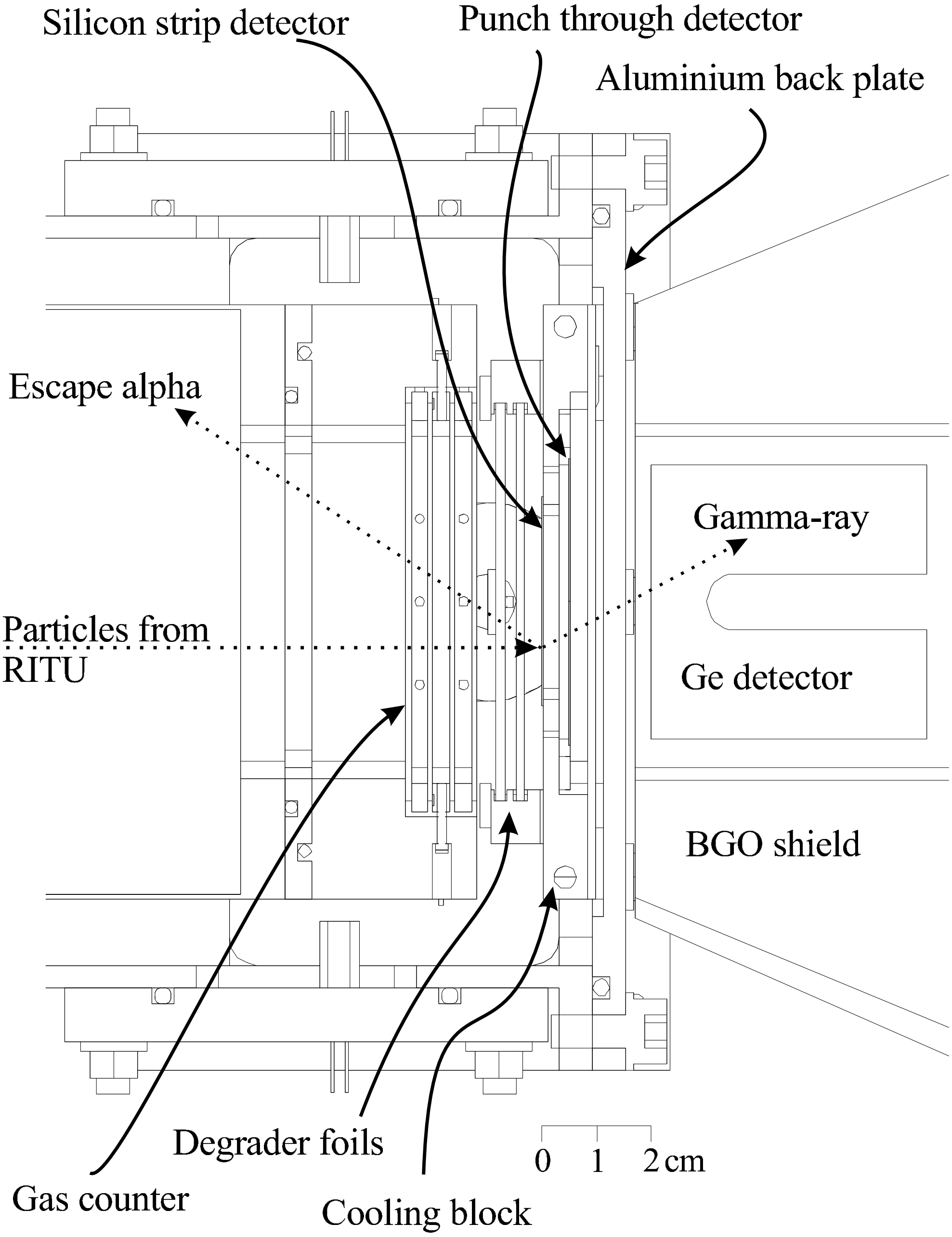

Figure 3.14: Arrangement of the detectors at the focal plane. A separated nucleus from RITU flies through the gas counter and is implanted into the silicon strip detector. After some time the nucleus alpha decays. In the case the alpha particle is emitted to the backward angles it is registered by the gas counter. In the case of alpha-gamma coincidence measurements the coincidence gamma-ray can be detected by the Ge-detector installed behind the detector chamber.

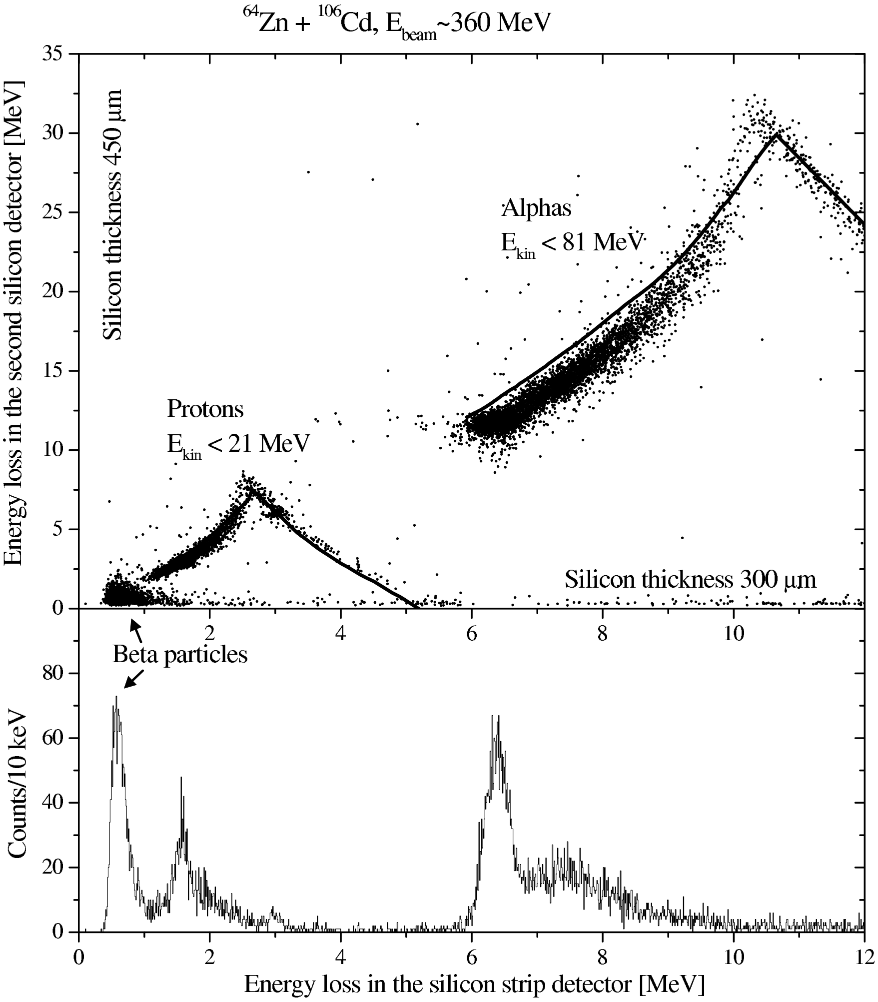

Figure 3.15: Upper panel shows the identification of the punch through particles using energy loss signals in the silicon detectors. Lower panel shows the energy loss spectrum of the particles in the silicon strip detector.

3.3.4 Detection of gamma- and X-rays at the focal plane

A Compton-suppressed Nordball-type germanium detector [Mos89] with relative efficiency of 40 % was installed behind the silicon detector (see figure 3.14). An absolute efficiency of $4.5 - 5.5\,\%$ was reached for the detection of gamma- and X-rays in the energy region of $80 - 200\,\mathrm{keV}$. The relative efficiency curve was measured according to the standard method using well-known gamma-ray intensities from a ^{133}Ba + ^{152}Eu source. The absolute efficiency was measured using a calibrated ^{60}Co source and well-known alpha-gamma coincidences observed in the measurements. The germanium detector was mainly used for the detection of the prompt and delayed (up to 8 μs) gamma- and X-rays arising after the alpha decay in the silicon strip detector. These coincidence measurements are illustrated in figure 3.16.

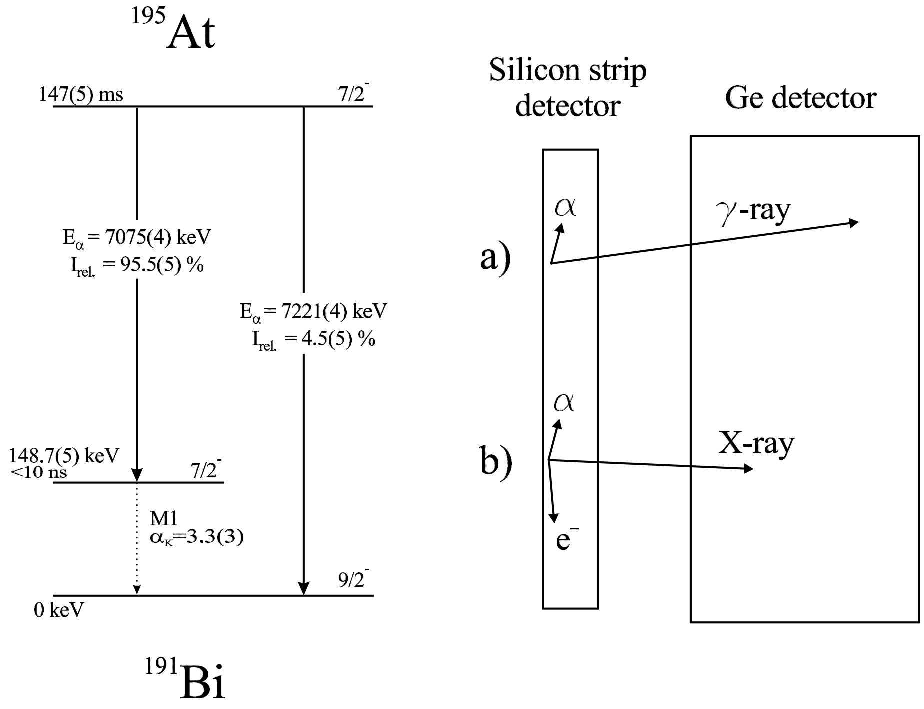

Figure 3.16: Schematic drawing illustrating coincidences of events in the silicon strip detector and the Ge detector. On the left hand side is shown the alpha-decay scheme of the $7/2^-$ state in ^{195}At. On the right hand side: a) alpha decay in the silicon detector coincident with a gamma-ray observed in the Ge detector. b) the M1 transition in the daughter nucleus is converted and the preceding alpha decay is in coincidence with the conversion electron in the silicon detector and the X-ray in the Ge detector. Due to the prompt de-excitation of the level in the daughter nucleus the energies of the alpha particle and the conversion electron are summed in the silicon detector.

When the state in the daughter nucleus de-excites via internal conversion the alpha-decay spectrum may look rather complicated as noticed in the alpha-decay studies of the $7/2^-$ state in ^{191}At, ^{193}At and ^{195}At (see publications **I** and **II**). This is due to the summing of the alpha-particle energy with the various possible conversion electron and X-ray energies in the silicon detector. In addition, the possibility that the conversion electrons may escape from the silicon detector and deposit only part of their kinetic energy into the detector complicates the decay energy spectrum. The summing of the alpha particle and the conversion electron energies in the heaviest elements is studied in reference [Heß89].

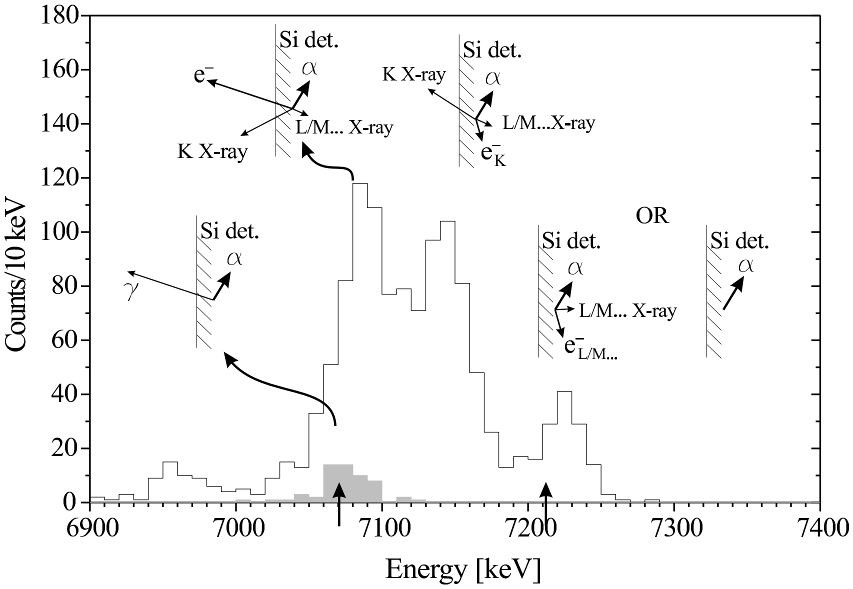

Figure 3.17: The energy spectrum of the correlated alpha decays of the $7/2^-$ state in ^{195}At illustrating the summing of the alpha particle and conversion electron energies. The arrows show the alpha-decay energies to the excited $7/2^-$ state and to the $9/2^-$ ground state in the daughter nucleus ^{191}Bi (see figure 3.16). The series of drawings visualises the de-excitation processes of the $7/2^-$ state in ^{191}Bi causing the structure to the energy spectrum. The filled area shows the energy spectrum of the alpha particles which were observed in coincidence with 148.7(5) keV gamma-ray events. (See text and publication **I** for more details.)

The summing of the alpha particle and conversion electron energies can be illustrated by the alpha decay of the $7/2^-$ state in ^{195}At. The energy spectrum of the decay events correlated with the recoil and the subsequent alpha decay of the $9/2^-$ ground state of ^{191}Bi is shown in figure 3.17. The energies of alpha decays to the isomeric state and directly to the ground state in ^{191}Bi are marked by arrows (see the decay scheme in figure 3.16). The filled area represents the energy spectrum of alpha particles detected in coincidence with 148.7(5) keV gamma-ray events in the Ge detector. These coincidences are shown in a two-dimensional plot in figure 3.18. The coincidences with the full-energy gamma-ray events ensure that no additional energy from conversion electron or X-ray cascades was summed up to the alpha-particle energy. Thus these events were used in the determination of the alpha-particle energy to the excited state at 148.7(5) keV in ^{191}Bi. Correspondingly, the peak around 7085 keV in figure 3.17 represents the alpha decay to the same excited state in ^{191}Bi. The energy shift of approximately 10 keV compared to the value determined from the alpha-gamma coincidences is caused by summing of the alpha-particle energy with the energy deposited by the escaped conversion-electron and the subsequent low-energy ($\lesssim 15\,\mathrm{keV}$) X-ray cascade ($300\,\mu$m of silicon is the half-thickness for a 15 keV gamma-ray). The alpha peak at 7140 keV can be explained by summing of the alpha-particle energy with the K conversion-electron energy and the following low-energy X-ray cascade. The alpha peak at 7220 keV can be explained by summing of the alpha energy of the decay to the $7/2^-$ excited state with the L or M conversion-electron energy and with the energy of the subsequent low-energy X-ray cascade or by alpha decay directly to the $9/2^-$ ground state in ^{191}Bi. As discussed in more detailed in publication **I** both of these possibilities contribute to the 7220 keV alpha peak in figure 3.17.

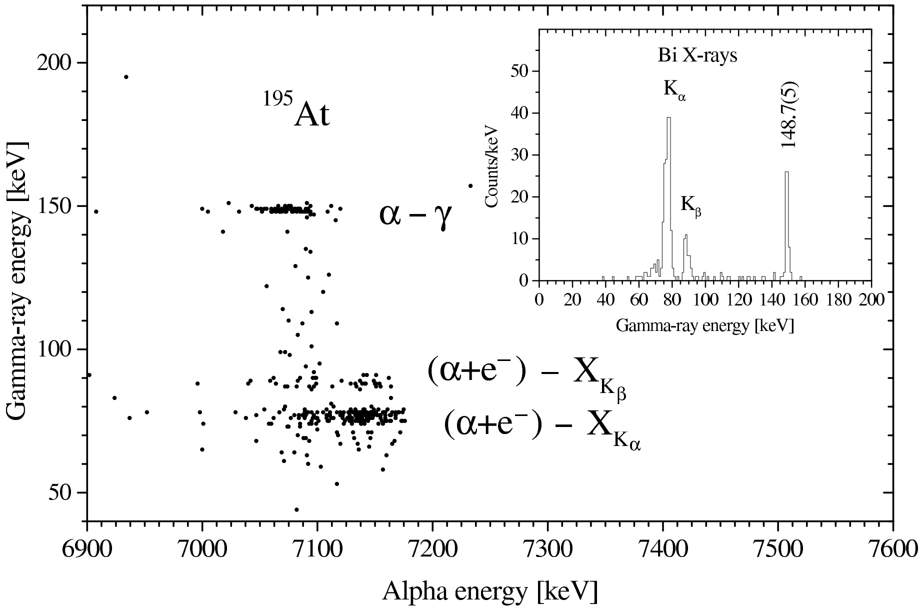

Figure 3.18: A two-dimensional plot of alpha-gamma coincidence events at the focal plane for the alpha decay of ^{195}At. The origin of the various coincidences is noted. In the events where the X-ray is observed in coincidence with an alpha particle the alpha energy is clearly shifted due to the summing of the alpha and the conversion-electron energies. The energy spectrum of the gamma- and X-ray events is shown in the inset panel. The intensity ratio of the gamma-rays and K X-rays after correction for the germanium detector efficiency can be used to determine the K conversion coefficient.

The alpha-decay studies of the odd-mass astatine isotopes presented in publications **I** and **II** are illustrative examples about the use of alpha-gamma coincidence measurements. Utilising this technique the complicated alpha-decay structures of ^{193}At and ^{195}At isotopes were clarified. Simultaneously, low-lying excited states in the corresponding daughter nuclei ^{189}Bi and ^{191}Bi were discovered.

In addition, the fairly flexible focal plane detector system allowed the use of a small detector chamber for the experiments where higher gamma-ray detection efficiency was required. In this construction five Compton-suppressed Ge detectors were arranged closely around the silicon detector as shown in figure 3.19. A high gamma-ray detection efficiency at the focal plane was needed especially in the experiments where alpha-gamma coincidences or isomeric states in recoils were searched for (for example recoil-isomer tagging). In addition, the use of five Ge-detectors around the silicon detector allowed the search for $\gamma\gamma$-coincidences at the focal plane.

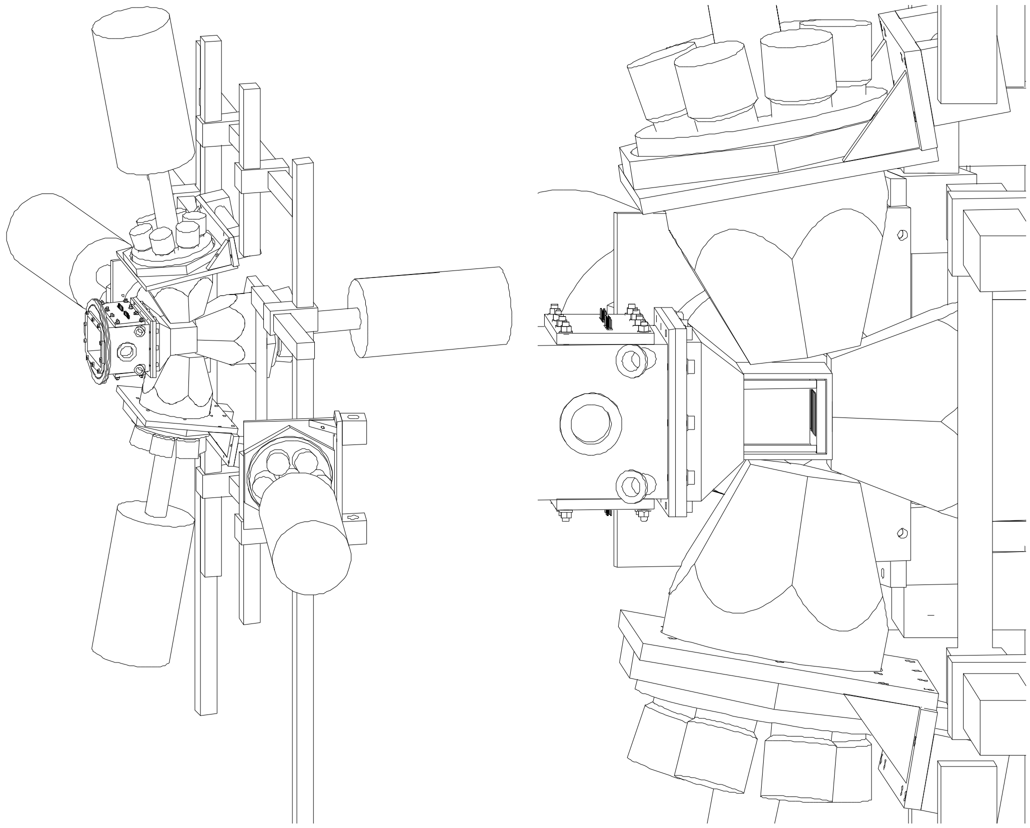

Figure 3.19: On the left the arrangement of the Ge detectors around the small focal plane detector chamber is shown. One Ge detector is retracted for easier viewing. On the right a closer view. The wall of the chamber is removed so that the position of the silicon detector can also be seen.

4 Summary of results

Here are presented some highlights of the experimental results obtained in the present work. More detailed discussions about the analysis and the results are presented in the enclosed articles. Overviews of the results and technical developments are also published in references [Ket01a, Ket03]. A summary of fusion-evaporation reactions used in the present work along with the measured production cross sections of the primary products is presented in table 4.1.

Table 4.1: Measured production cross-sections of the reactions used in the present work. Beam energies in the middle of the target are given. The ^{195}At experiment was dedicated to the production of a new radon isotope ^{195}Rn [Ket01b] and the astatine isotope was obtained as a side-product. As a comparison the cross section for a better reaction for ^{195}At production is shown [Enq96] (marked by *). A transmission of 40 % for evaporation residues was assumed.

Nucleus	Reaction	Cross-section	Beam energy
^{171}Au	$^{78}\mathrm{Kr} + {}^{96}\mathrm{Ru} \rightarrow {}^{171}\mathrm{Au} + \mathrm{p2n}$	$1.1\,\mu$b	359 MeV
^{170}Au	$^{78}\mathrm{Kr} + {}^{96}\mathrm{Ru} \rightarrow {}^{170}\mathrm{Au} + \mathrm{p3n}$	90 nb	386 MeV
^{176}Tl	$^{78}\mathrm{Kr} + {}^{102}\mathrm{Pd} \rightarrow {}^{176}\mathrm{Tl} + \mathrm{p3n}$	3 nb	384 MeV
^{195}At*	$^{56}\mathrm{Fe} + {}^{141}\mathrm{Pr} \rightarrow {}^{195}\mathrm{At} + 2\mathrm{n}$	900 nb	230 MeV
^{195}At	$^{56}\mathrm{Fe} + {}^{142}\mathrm{Nd} \rightarrow {}^{195}\mathrm{At} + \mathrm{p2n}$	200 nb	262 MeV
^{193}At	$^{56}\mathrm{Fe} + {}^{141}\mathrm{Pr} \rightarrow {}^{193}\mathrm{At} + 4\mathrm{n}$	40 nb	266 MeV
^{191}At	$^{54}\mathrm{Fe} + {}^{141}\mathrm{Pr} \rightarrow {}^{191}\mathrm{At} + 4\mathrm{n}$	300 pb	260 MeV

4.1 Odd-mass At isotopes beyond the proton drip line

Alpha-decay properties of the new isotope ^{191}At were investigated for the first time and the decay properties of ^{193}At and ^{195}At were studied with improved accuracy. New information concerning the low-lying states in the corresponding daughter nuclei ^{187}Bi, ^{189}Bi and ^{191}Bi was also gained. The previous

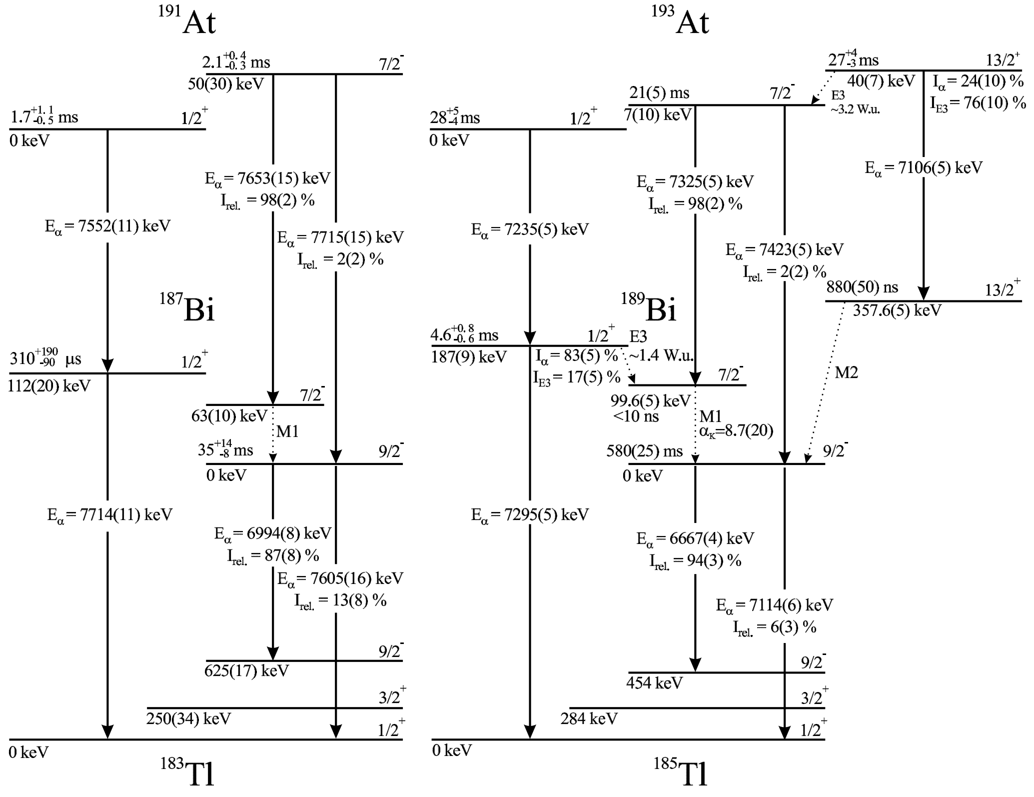

Figure 4.1: Proposed alpha-decay schemes of ^{191}At and ^{193}At. The decay properties of the $13/2^+$ state shown for ^{189}Bi were taken from refs. [And01, Hür02]. (^{a}): this is the corrected value, the measured value without correction is $(31.8^{+1.5}_{-1.3})$ ms. See publication **II** for more details.

alpha-decay studies of ^{193}At were presented in references [Enq96, Lei95b]. A summary of the previous studies of ^{195}At is presented in the introduction part of publication **I**.

The decay schemes suggested for ^{191}At, ^{193}At and ^{195}At based on the present results are shown in figures 4.1 and 4.2. As a comparison the decay scheme of ^{197}At [Coe86] is also shown in figure 4.2. Three alpha-decaying states were identified for ^{193}At, and two for both ^{191}At and ^{195}At nuclei. For each of these isotopes the $1/2^+$ intruder state was observed to be the ground state, though in ^{193}At also the $7/2^-$ state could be the ground state within the accuracy of the measurement. The alpha decays of the $7/2^-$ states in ^{195}At and ^{193}At were observed to feed the excited $7/2^-$ states at 148.7(5) keV and 99.6(5) keV in the corresponding daughter nuclei ^{191}Bi and ^{189}Bi, respectively. The spin, parity and excitation energy of these final states, observed for the first time, were determined using the properties of gamma-ray transitions observed in coincidence with the alpha decay of the ^{195}At and ^{193}At isotopes.

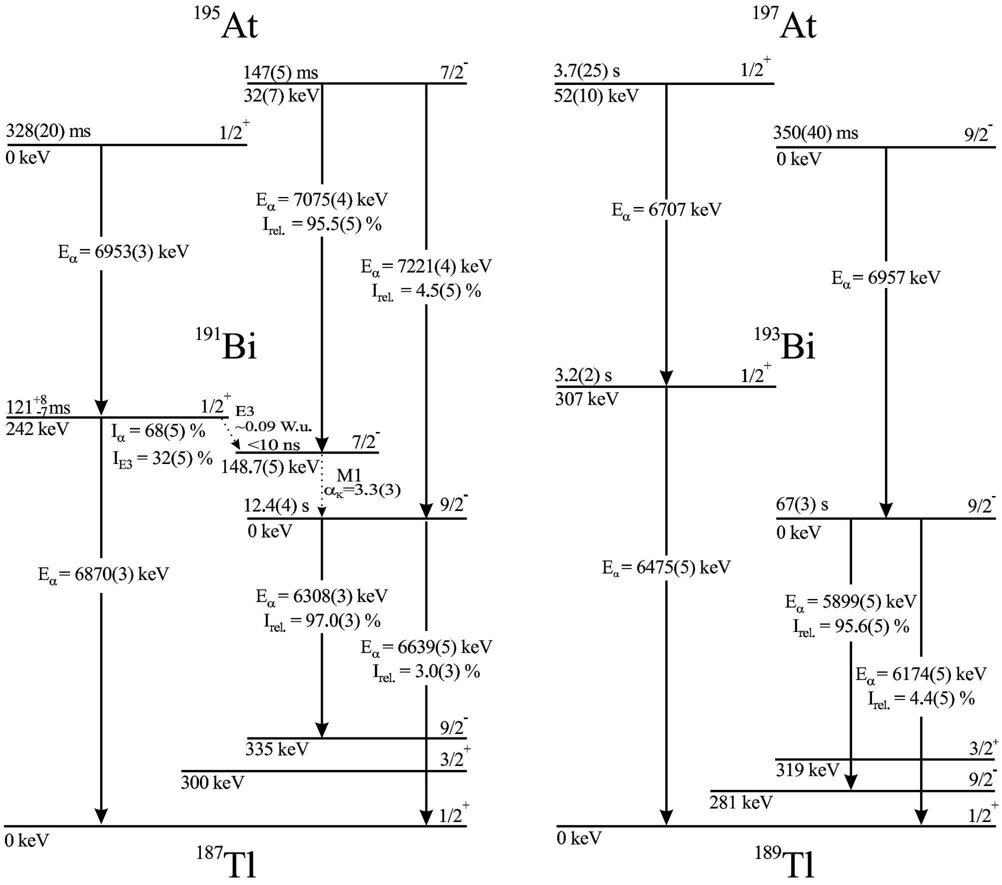

Figure 4.2: The decay properties and low-lying levels in ^{195}At and ^{197}At and in the corresponding daughter nuclei ^{191}Bi and ^{193}Bi. The data shown for ^{197}At, ^{193}Bi and the properties of ground state to ground state decay in ^{191}Bi are taken from references [Coe85, Coe86]. See publication **I** for more details.

The identification of the $13/2^+$ state in ^{193}At was also based on alpha-gamma coincidences. In ^{187}Bi the existence of the excited $7/2^-$ state at 63(10) keV was deduced based on the shape of the alpha-decay energy spectrum of ^{191}At and the systematics of the heavier odd-mass bismuth isotopes. The spin and parity assignments of the initial states in the astatine isotopes were based on the unhindered alpha decays.

The level systematics of the odd-mass bismuth and astatine isotopes are shown in figure 4.3. For astatine isotopes the systematics are obtained by using proton binding energies and normalising them to the ground state of the bismuth isotopes. This is done to illustrate the behaviour of the states in light astatine isotopes where they cannot be compared to the $9/2^-$ ground state as in the heavier isotopes. The mass values needed for the pro-

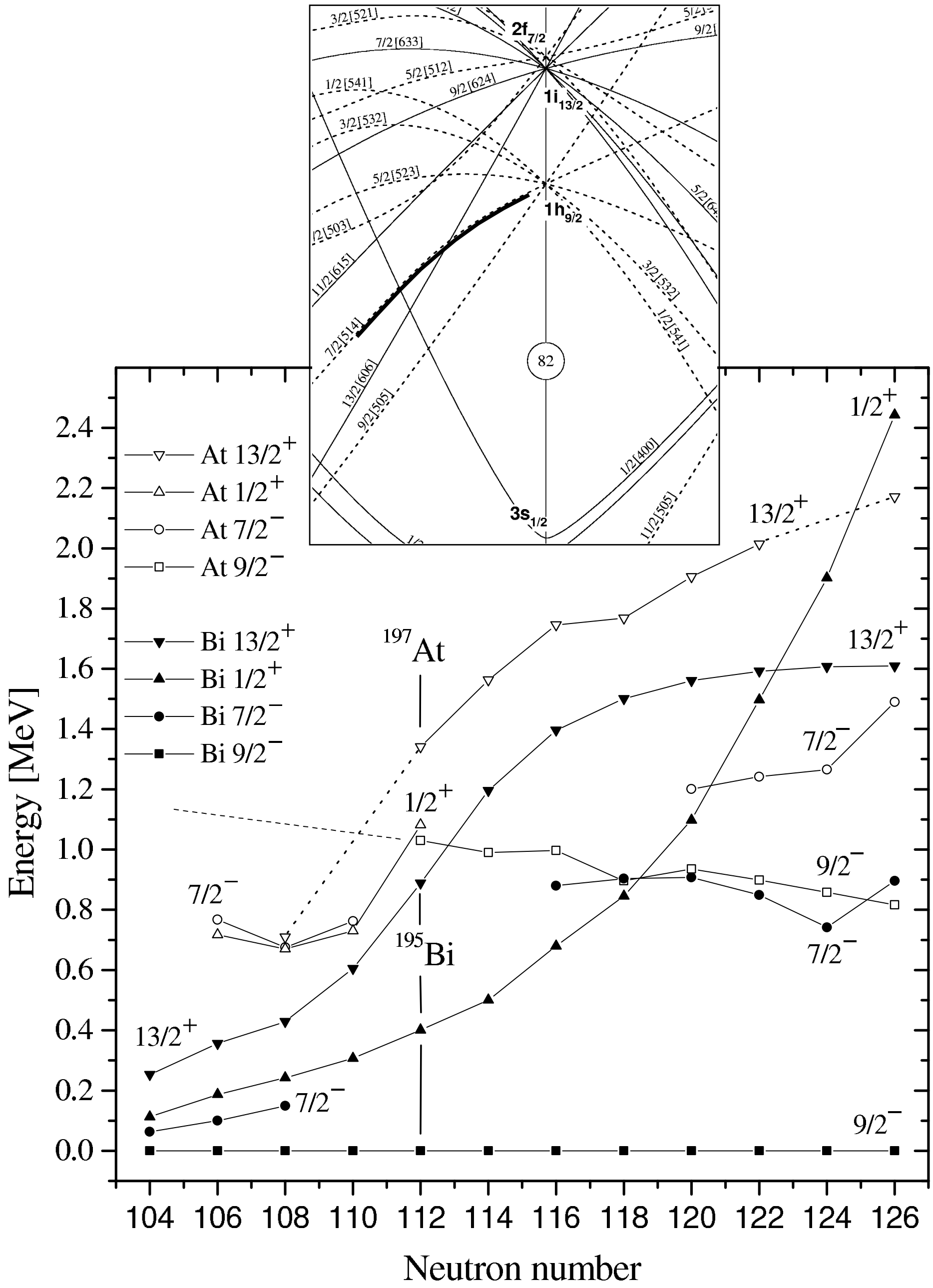

Figure 4.3: The level systematics of odd-mass bismuth and astatine isotopes. The systematics for astatine isotopes are obtained by normalising the proton binding energies to the ground state of the bismuth isotopes. See text and publication **II** for more details. The upper panel shows the Nilsson diagram for protons in the lead region. The emphasized Nilsson orbital 7/2$^-$[514] is associated with the existence of a low-lying 7/2$^-$ state in light odd-mass bismuth and astatine isotopes.

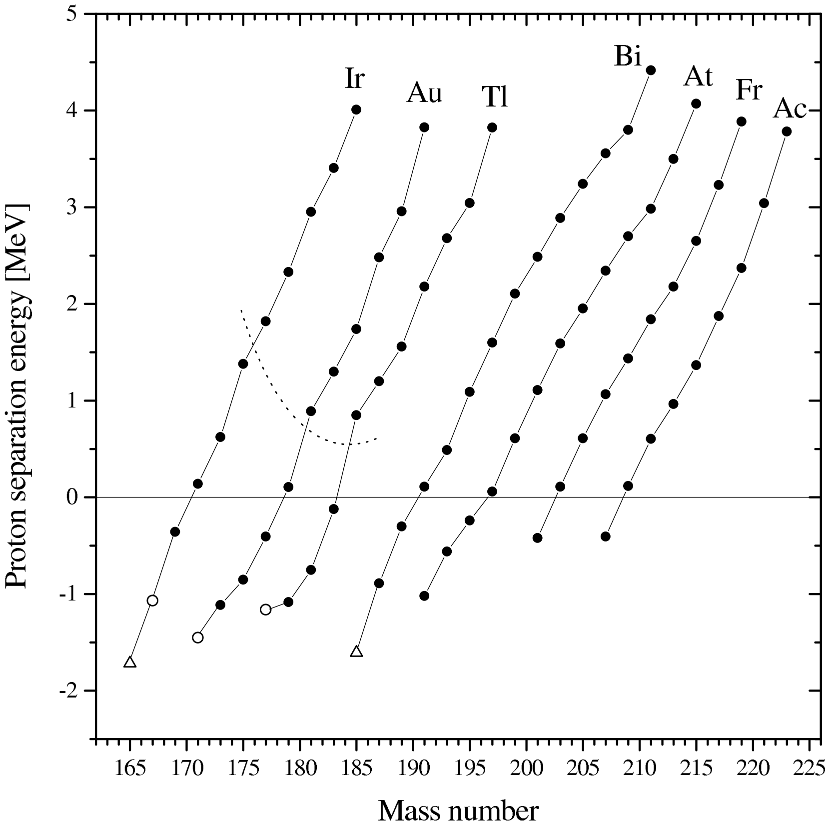

Figure 4.4: Proton separation energies for odd-mass isotopes from Ir to Ac. The filled circles denote energies derived from measured atomic masses in references [Rad00, Nov02], except for Ac and Fr isotopes and for Tl, Au and Ir isotopes below the dotted line for which the masses given in reference [Aud97] were used. The open circles represent the measured proton separation energies for the ground state to ground state proton emissions [Dav97, Pol99]. The open triangles represent the measured proton separation energies, but in these cases the proton emission most probably originates from an excited state [Dav96, Pol01].

ton binding energies were taken from the recent atomic mass measurements [Nov02, Rad00, Aud97], updated with the new results for ^{191}At, ^{193}At, ^{195}At and ^{187}Bi obtained in the present work. An overall accuracy of approximately 100 keV was given for the measured masses.

The level schemes suggested for ^{191}At, ^{193}At and ^{195}At were observed to differ from those observed in heavier odd-mass astatine isotopes from ^{197}At to ^{211}At (see figures 4.1, 4.2 and 4.3). The intruder $1/2^+$ state, having a $\pi(4p-1h)$ configuration becomes the ground state in ^{195}At. In the heavier odd-mass astatine isotopes, the ground state is the $9/2^-$ state with $(\pi h_{9/2})^3$ configuration. In addition, a $7/2^-$ state rather than a $9/2^-$ state was suggested to represent the first excited state in these light astatine isotopes. The emergence of the $7/2^-$ state over the $9/2^-$ state can be understood by assuming a change in deformation of this three-particle configuration between the ^{197}At and ^{195}At isotopes. Since no sizeable ground state deformation was observed in ^{197}At [Smi99] the last proton in the $\pi h_{9/2}$ orbital creates the $9/2^-$ ground state. According to the Nilsson diagram (see figure 4.3) a $7/2^-$ state, associated with an oblate $7/2^-[514]$ Nilsson state, originating predominantly from the $\pi h_{9/2}$ orbital at sphericity and having a mixed $\pi f_{7/2}/\pi h_{9/2}$ character at oblate deformation, becomes available for the 85th proton in odd-mass astatine isotopes if sufficient oblate deformation is assumed. Based on the results of the present work it is proposed that the deformed three-particle configuration, driving the last proton to the $7/2^-[514]$ Nilsson state, is energetically more favoured than the nearly spherical $(\pi h_{9/2})^3$ configuration in light $A < 197$ odd-mass astatine isotopes. A change in the ground state deformation from a nearly spherical shape to an oblate shape is theoretically predicted to happen between ^{199}At and ^{198}At by Möller *et al.* in reference [Möl95]. Correspondingly, the existence of a low-lying $7/2^-$ state in bismuth isotopes can be understood by a $7/2^-[514]$ Nilsson proton state associated with oblate deformed structures.

The 148.7(5) keV gamma-ray transition associated with the de-excitation of the $7/2^-$ state in ^{191}Bi was also observed in an in-beam gamma-ray measurement [Nie03]. The recent potential energy calculations presented in that paper and in reference [And03] support the $7/2^-$ assignment of this low-lying state observed in ^{189,191}Bi and deduced to exist in ^{187}Bi. Based on these calculations this state in ^{189,191}Bi was associated with the oblate $7/2^-[514]$ configuration as deduced also in the present work. At the mid-shell nucleus ^{187}Bi$_{104}$ the excitation energy of the $7/2^-$ state was still observed to come down (see systematics in figure 4.3). However, according to the calculations [And03] the excitation energy of the oblate structure should already increase in ^{187}Bi. The downward behaviour was explained by a prolate $7/2^-$ state, originating from the $1/2^-[530]$ orbital, which crosses the oblate configuration between ^{189}Bi and ^{187}Bi. In addition, similar crossing of the oblate and prolate structures is most likely occurring in the $1/2^+$ and $13/2^+$ states [And03].

The proton separation energies of astatine isotopes, shown in figure 4.4, decrease smoothly with decreasing mass number until the first clearly proton unbound isotope ^{195}At is reached. The graph behaves like the two curves would cross between ^{197}At and ^{195}At. This is indeed true, since the change in the ground state assignment from a $9/2^-$ state to a $1/2^+$ state (see figure 4.3) causes the bend in the proton separation energy systematics. Surprisingly, a similar, but weaker bend can also be seen in the proton separation energy systematics of bismuth isotopes. In analogy to astatine isotopes it may indicate a change also in the structure of bismuth isotopes. However, a possible inaccuracy in the present atomic mass data, used for the plot, cannot be fully excluded.

Proton separation energies of −240(130) keV, −560(140) keV and −1020(140) keV were determined for ^{195}At, ^{193}At and ^{191}At, respectively. This indicates that ^{195}At is the first proton unbound astatine isotope. The proton separation energy obtained for ^{191}At would correspond to a partial half-life of approximately 57 s for an unhindered proton emission from the $\pi s_{1/2}$ orbital. This is calculated using the WKB barrier transmission approximation through the real part of a Becchetti-Greenlees optical potential [Bec69] and using a spectroscopic factor of one. Although the WKB approximation is very rough and works mainly for spherical nuclei, it shows that the branching ratio of the proton emission compared to the alpha-decay would be too small for detection. By extrapolating the systematics obtained for the heavier At isotopes the proton separation energy of the next odd-mass astatine isotope ^{189}At can be estimated to be approximately −1500 keV (see figure 4.4). Based on the WKB calculation this value would correspond to a half-life of approximately 50 μs for proton emission from the $\pi s_{1/2}$ orbital assuming a spectroscopic factor of one. An energy of 7900 keV can be extrapolated for the alpha decay of $1/2^+$ state in ^{189}At to the $1/2^+$ state in ^{185}Bi. This value would correspond to a partial half-life of 400 μs for an unhindered alpha decay. Thus, the ^{189}At nucleus is a good candidate for the observation of proton emission in astatine isotopes.

4.2 Proton emission in ^{170}Au and ^{176}Tl nuclei

Decay studies of the previously known proton emitting nuclei ^{171}Au and ^{170}Au [Dav97, Pol99, Bäc03, Mah02] were performed with improved accuracy and the decay of the ground state in ^{170}Au was observed for the first time. In addition, a short test experiment for the production of a new proton emitting nucleus ^{176}Tl was performed and the proton emission from the ground state was identified. The decay of an isomeric state in the previously known proton emitter ^{177}Tl [Pol99] was also observed in this experiment. In addition, the alpha decay of the new ^{171}Hg isotope was identified and the decay properties of previously known ^{172,173}Hg [Sew99] and ^{167,168,169,170}Pt [Bin96, Pag96] isotopes were also measured.

Two proton emitting and alpha decaying states were identified for the ^{170}Au nucleus. Both proton radioactivities were observed to feed the ground state in ^{169}Pt. The ordering of the states and the excitation energy of 282(10) keV

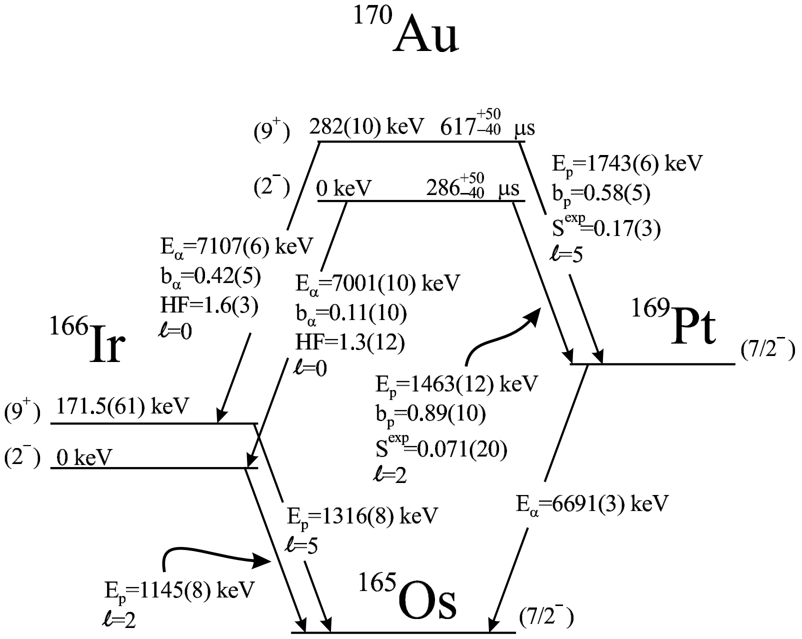

Figure 4.5: Decay scheme obtained for ^{170}Au in the present work. Data shown for ^{166}Ir are taken from reference [Dav97].

for the isomeric state was concluded based on the proton emission Q-values. The alpha-decaying states were linked with the corresponding proton emitting states using the half-life and the Q-value examination. The decay scheme obtained for ^{170}Au is shown in figure 4.5.

A low-seniority shell-model calculation introduced in reference [Dav97] predicts that the spectroscopic factor S^{calc} for proton emission in Au isotopes is 0.22 when near degeneracy between $s_{1/2}$, $d_{3/2}$ and $h_{11/2}$ proton orbitals is assumed. This indicates that the proton half-lives calculated using the WKB barrier transmission approximation should be shorter than the measured values. Based on the experimental spectroscopic factors the ground state proton emission in ^{170}Au was concluded to represent an $\ell = 2$ transition indicating that the proton is emitted from a $\pi d_{3/2}$ orbital. Correspondingly, the proton emission from the isomeric state can be explained with an $\ell = 5$ transition corresponding to a proton emission from a $\pi h_{11/2}$ orbital. The results indicate, that the structures of the ground and the isomeric state in ^{170}Au are similar to the corresponding states in the alpha decay daughter nucleus ^{166}Ir [Dav97].

The alpha-decay hindrance factors of the present work were calculated according to the method of Rasmussen [Ras59] and normalised to the alpha decay of ^{212}Po. The hindrance factors of 1.3(12) and 1.6(3) obtained for the alpha decay of the ground state and the isomeric state, respectively, in ^{170}Au show both an unhindered character. This is in agreement with the conclusion based on the proton emission that the structures of the ground states and the isomeric states in ^{170}Au and in the alpha decay daughter nucleus ^{166}Ir are similar. Thus, based on the configurations given for ^{166}Ir in reference [Dav97], $[\pi d_{3/2}\nu f_{7/2}]_{2^-}$ and $[\pi h_{11/2}\nu f_{7/2}]_{9^+}$ configurations were suggested for the ground state and the isomeric state in ^{170}Au, respectively.

One decay branch was identified to originate from the new proton emitting nucleus ^{176}Tl as shown in figure 4.6. The low-seniority shell-model calculation [Dav97] predicts that the spectroscopic factor S^{calc} for proton emission in Tl isotopes is 0.11. However, it might be that the assumption of nearly degenerate $s_{1/2}$, $d_{3/2}$ and $h_{11/2}$ proton orbitals does not necessarily hold in the case of light thallium isotopes, since the energy difference between the low and high spin states associated with $s_{1/2}$ and $h_{11/2}$ proton orbitals is quite large. For example in the lightest previously known thallium isotope ^{177}Tl the energy difference between the states is already approximately 800 keV as discussed in reference [Pol99]. However, based on the spectroscopic factor examination the proton emission observed for ^{176}Tl was concluded to originate from an $s_{1/2}$ proton orbital. Thus the proton emission represents the decay of the low-spin state which can be associated with the ground state configuration in light thallium isotopes.

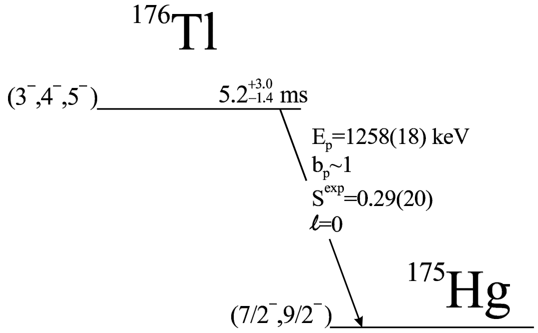

Figure 4.6: Decay scheme obtained for ^{176}Tl.

The high-spin states should be fed more strongly than the low-spin states in the heavy ion fusion reaction. However, the decay of a possible high-spin state in ^{176}Tl where the proton can be expected to be emitted from an $h_{11/2}$ orbital was not observed. The reason is most probably the half-life which is too short to be detected with the data acquisition system used in the present experiment. In addition, a possibility of gamma-ray de-excitation of the state cannot be excluded.

By taking into account the dead time of the data acquisition system (approximately 15 μs) it is possible to estimate the lowest limit for the excitation energy of the high-spin state. Since no proton emission was observed from an $h_{11/2}$ proton orbital it can be estimated that the half-life of the state should be at least three times shorter than the dead time. Based on the WKB approximation the lowest limit for the excitation energy of the high-spin state (proton emission from an $h_{11/2}$ orbital) is approximately 950 keV, when a 5 μs upper limit for the half-life and a spectroscopic factor of 0.11 were assumed. The estimated lower limit for the excitation energy is in agreement with the excitation energy observed for ^{177}Tl [Pol01].

The observation of the ground-state proton emission from an $s_{1/2}$ orbital in ^{176}Tl differs from that observed for the lighter odd-odd proton emitting nuclei ^{156}Ta [Liv93b], ^{160}Re [Woo97], ^{166}Ir [Dav97] and ^{170}Au (the present work). In these nuclei the ground state proton emission has been deduced to occur from a $d_{3/2}$ proton orbital which was suggested to be coupled to an $f_{7/2}$ neutron. In ^{176}Tl$_{95}$ there are two orbitals, $\nu f_{7/2}$ and $\nu h_{9/2}$, available for the odd neutron. By coupling these neutrons with a proton in the $\pi s_{1/2}$ orbital the $[\pi s_{1/2}\nu f_{7/2}]_{3^-,4^-}$ and $[\pi s_{1/2}\nu h_{9/2}]_{4^-,5^-}$ configurations are obtained, respectively. Since the coupling properties of the odd proton and the odd neutron in such neutron-deficient Tl isotopes are not very well known, no definitive conclusion about the ground state spin and parity assignment could be drawn based on the present data. However, the change in the ground-state proton configuration in ^{176}Tl compared to the lighter odd-odd proton emitters may indicate that the $\nu h_{9/2}$ orbital plays a role in the ground state of ^{176}Tl.

5 Conclusion

During the past few years the decay spectroscopy of neutron deficient nuclei above the $N = 82$ neutron shell closure and beyond the proton drip line has been one of the main goals of studies performed at the gas-filled recoil separator RITU. To reach this extreme limit of the capability of the experimental devices, several technical developments have taken place at the separator. An improved focal plane detector system was constructed taking into account the special needs of proton decay studies. The dipole chamber and the beam stop of the separator were redesigned for better suppression of the beam particles. A beam-windowless helium filling-gas differential pumping system was installed in order to allow the use of higher beam intensities, which were needed especially for the decay studies of nuclei above the $Z = 82$ proton shell closure and beyond the proton drip line. These improvements have made the gas-filled recoil separator RITU at least an order of magnitude more sensitive and widened its working area from heaviest elements close to the ^{100}Sn region.

The technical developments of the gas-filled recoil separator RITU have allowed the detailed studies of the neutron deficient odd-mass astatine isotopes beyond the proton drip line. Earlier unclear decay properties of ^{193,195}At isotopes are now clarified using the sensitive alpha-gamma coincidence method. In addition, the alpha decay of the next odd-mass astatine isotope ^{191}At was also studied. The level schemes of these nuclei are suggested to differ from those observed in heavier odd-mass astatine isotopes. For each of these isotopes the oblate $1/2^+$ intruder state was observed to be the ground state instead of the nearly spherical $9/2^-$ state which is the ground state in the heavier odd-mass astatine isotopes. In addition, a $7/2^-$ state rather than the $9/2^-$ state is suggested to represent the first excited state in these light odd-mass astatine isotopes. Correspondingly, a new low-lying $7/2^-$ state, fed by the alpha decay of the astatine isotopes, was observed via gamma-ray de-excitation in ^{189,191}Bi isotopes. The existence and the excitation energy of this state in ^{187}Bi was deduced based on the shape of the alpha-decay spectrum of ^{191}At and the systematics in the heavier odd-mass bismuth isotopes. The emergence of a low-lying $7/2^-$ state in light odd-mass At and Bi isotopes was understood via the $7/2^-[514]$ Nilsson proton orbital associated with an oblate deformed structure. Based on the experimental results, the $7/2^-$ state is observed coming down in excitation energy even in ^{187}Bi. Thus, the state may play a vital role in the decay scheme of the proton emitting nucleus ^{185}Bi.

The decay properties of several neutron-deficient Pt, Au, Hg and Tl nuclei have also been studied. In the proton-emitting ^{170}Au nucleus, the ground-state proton emission and alpha decay were observed for the first time and the decay properties of the isomeric state were measured with improved accuracy. The decay of the proton-emitting ^{171}Au nucleus was measured with high statistics. The alpha decay of the new isotope ^{171}Hg was observed and the decay properties of the previously known ^{172,173}Hg and ^{167,168,169,170}Pt nuclei were also measured. Ground-state proton emission was identified in the new thallium isotope ^{176}Tl. As a side-product of the measurement the decay of the proton-emitting ^{177}Tl nucleus was also detected.

A WKB barrier transmission approximation was used to calculate the proton emission probabilities. The experimental spectroscopic factors were compared to values predicted by a low-seniority shell model calculation assuming a near degeneracy of the $s_{1/2}$, $d_{3/2}$ and $h_{11/2}$ proton orbitals. As a result, the proton orbitals of the parent nuclei involved in the proton emission were deduced. A change in the ground state proton configurations in odd-odd nuclei between ^{170}Au and ^{176}Tl is suggested. The results illustrate the sensitivity of the proton emission and the variety of spectroscopic information that can be obtained via proton emitting nuclei beyond the proton drip line.

The results of the present work encourage to continue the studies of nuclei in the vicinity of the lead region and beyond the proton drip line. For comprehensive and more difficult measurements the focal plane detector system has recently been upgraded by the GREAT (Gamma Recoil Electron Alpha Tagging) spectrometer [Pag03]. The spectrometer increases the sensitivity of the focal plane detector system facilitating the detection of weak reaction channels. Due to the high granularity the reduction of the background events using the correlation and coincidence methods is considerably improved. An important part of the GREAT setup is the Total Data Readout (TDR) data acquisition system which is based on VXI-electronics and designed to minimise the dead time of the acquisition process. Instead of using a common master trigger for reading out the ADC channels, all the channels are running independently. The data are associated and time-stamped by software using a global 100 MHz clock. For in-beam gamma-ray experiments the JuroGam array has recently been combined with the RITU separator. The array consists of 43 Eurogam Phase I Ge detectors providing a photopeak efficiency of 4.2 % at 1.3 keV.

In near future, the level structure of ^{195}At, which is the subject of publication **I**, will be probed employing the $\mathrm{JuroGam}-\mathrm{RITU}-\mathrm{GREAT}$ setup. This measurement will provide more detailed information on the intruder states discussed in the present work. Also the $9/2^-$ and $13/2^+$ states known in heavier nuclei could possibly be observed in this measurement. In addition to remeasuring the $^{187-193}$Bi isotopes with higher statistics, in-beam gamma-ray measurements are now proposed to be extended to the heaviest known proton emitting nucleus ^{185}Bi. The behaviour of the low-lying $7/2^-$ state and its contribution to the decay scheme of the nucleus could be clarified in this measurement. Also the prolate structures predicted by the theoretical calculation [And03] could be searched for.

A challenging task will be the decay spectroscopy of the ^{192,194,196}At isotopes. In these measurements the high efficiency of gamma-ray detection at the focal plane provided by the GREAT spectrometer is crucial. Also the detection of conversion electrons in coincidence with alpha decays is useful. The level schemes observed in odd-mass At isotopes in the present work offer a basis for the alpha-decay studies of the neutron deficient Fr isotopes. In addition, decay studies of Au, Tl, Bi and At isotopes beyond the proton drip line will continue with the aim of the identification of ^{189}At via proton emission.

Bibliography

[Ako98] Y.A. Akovali, Nuclear Data Sheets **84**, (1998) 1.

[All98] R.G. Allatt, R.D. Page, M. Leino, T. Enqvist, K. Eskola, P.T. Greenlees, P. Jones, R. Julin, P. Kuusiniemi, W.H. Trzaska and J. Uusitalo, Phys. Lett. B **437**, (1998) 29.

[And99] A.N. Andreyev, D. Ackermann, P. Cagarda, J. Gerl, F.P. Heßberger, S. Hofmann, M. Huyse, A. Keenan, H. Kettunen, A. Kleinböhl, A. Lavrentiev, M. Leino, B. Lommel, M. Matos, G. Münzenberg, C. Moore, C.D. O'Leary, R.D. Page, S. Reshitko, S. Saro, C. Schlegel, H. Schaffner, M. Taylor, P. Van Duppen, L. Weissman and R. Wyss, Eur. Phys. J. A **6**, (1999) 381.

[And00] A.N. Andreyev, M. Huyse, P. Van Duppen, L. Weissman, D. Ackermann, J. Gerl, F.P. Heßberger, S. Hofmann, A. Kleinböhl, G. Münzenberg, S. Reshitko, C. Schlegel, H. Schaffner, P. Cagarda, M. Matos, S. Saro, A. Keenan, C. Moore, C.D. O'Leary, R.D. Page, M. Taylor, H. Kettunen, M. Leino, A. Lavrentiev, R. Wyss and K. Heyde, Nature **405**, (2000) 430.

[And01] A.N. Andreyev, D. Ackermann, P. Cagarda, J. Gerl, F.P. Heßberger, S. Hofmann, M. Huyse, A. Keenan, H. Kettunen, A. Kleinböhl, A. Lavrentiev, M. Leino, B. Lommel, M. Matos, G, Münzenberg, C. J. Moore, C. D. O'Leary, R.D. Page, S. Reshitko, S. Saro, C. Schlegel, H. Schaffner, M.J. Taylor, P. Van Duppen, L. Weissman and R. Wyss, Eur. Phys. J. A **10**, (2001) 129.

[And03] A.N. Andreyev, D. Ackermann, F.P. Heßberger, K. Heyde, S. Hofmann, M. Huyse, D. Karlgren, I. Kojouharov, B. Kindler, B. Lommel, G. Münzenberg, R.D. Page, K. Van de Vel, P. Van Duppen, W.B Walters and R. Wyss, to be published.

[Aud97] G. Audi, O. Bersillon, J. Blachot and A.H. Wapstra, Nucl. Phys. A **624**, (1997) 1.

[Bas80] Reiner Bass, *Nuclear Reactions with Heavy Ions*, Springer-Verlag, Berlin 1980.

[Bat99] J.C. Batchelder, K.S. Toth, C.R. Bingham, L.T. Brown, L.F. Conticchio, C.N. Davids, R.J. Irvine, D. Seweryniak, W.B. Walters, J. Wauters, E.F. Zganjar, J.L. Wood, C. DeCoster, B. Decroix and K. Heyde, Eur. Phys. J. A **5**, (1999) 49.

[Bec69] F.D. Becchetti and G.W. Greenlees, Phys. Rev. **182**, (1969) 1190.

[Ben84] R. Bengtsson, P. Möller, J. R. Nix and Jing-ye Zhang, Phys. Scr. **29**, (1984) 402.

[Ben89] R. Bengtsson, and W. Nazarewicz, Z. Phys. A **334**, (1989) 269.

[Bet37] H.A. Bethe, Rev. Mod. Phys. **9** (1937) 69.

[Bin96] C.R. Bingham, K.S. Toth, J.C. Batchelder, D.J. Blumenthal, L.T. Brown, B.C. Busse, L.F. Conticchio, C.N. Davids, T. Davinson, D.J. Henderson, R.J. Irvine, D. Seweryniak, W.B. Walters, P.J. Woods and B.E. Zimmerman, Phys. Rev. C **54**, (1996) R20.

[Boh69] Aage Bohr and Ben R. Mottelson, *Nuclear Structure*, W.A. Benjamin, New York, 1969, Vol. 1.

[Bäc03] T. Bäck, B. Cederwall, K. Lagergren, R. Wyss, A. Johnson, D. Karlgren, P. Greenlees, D. Jenkins, P. Jones, D.T. Joss, R. Julin, A. Keenan, H. Kettunen, P. Kuusiniemi, M. Leino, A.-P. Leppänen, M. Muikku, P. Nieminen, J. Pakarinen, P. Rahkila and J. Uusitalo, Eur. Phys. J. A **16**, (2003) 489.

[Cer70] J. Cerny, J.E. Esterl, R.A. Gough and R.G. Sextro, Phys. Lett. **33B**, (1970) 284.

[Cer72] J. Cerny, R. A. Gough, R. G. Sextro and J.E. Esterl, Nucl. Phys. **A188** (1972) 666.

[Coe85] E. Coenen, K. Deneffe, M. Huyse, P. Van Duppen and J.L. Wood, Phys. Rev. Lett. **54**, (1985) 1783.

[Coe86] E. Coenen, K. Deneffe, M. Huyse, P. Van Duppen and J.L. Wood, Z. Phys. A **324**, (1986) 485.

[Cre91] J. Cresswell, Eurogam project documentation, EDOC073, Nuclear Structure Software Support Group, Liverpool University, February 1991.

[Dav96] C.N. Davids, P.J. Woods, H.T. Penttilä, J.C. Batchelder, C.R. Bingham, D.J. Blumenthal, L.T. Brown, B.C. Busse, L. F. Conticchio, T. Davinson, D.J. Henderson, R.J. Irvine, D. Seweryniak, K.S. Toth, W.B. Walters and B.E. Zimmerman, Phys. Rev. Lett. **76**, (1996) 592.

[Dav97] C.N. Davids, P.J. Woods, J.C. Batchelder, C.R. Bingham, C.J. Blumenthal, L.T. Brown, B.C. Busse, L.F. Conticchio, T. Davinson, S.J. Freeman, D.J. Henderson, R.J. Irvine, R.D. Page, H.T. Penttilä, D. Seweryniak, K.S. Toth, W.B. Walters and B.E. Zimmerman, Phys. Rev. C **55**, (1997) 2255.

[Dav98] C.N. Davids, P.J. Woods, D. Seweryniak, A.A. Sonzogni, J.C. Batchelder, C.R. Bingham, T. Davinson, D.J. Henderson, R.J. Irvine, G.L. Poli, J. Uusitalo and W.B. Walters, Phys. Rev. Lett. **80**, (1998) 1849.

[Dav00] Cary N. Davids and Henning Esbensen, Phys. Rev. C **61**, (2000) 054302.

[Dob02] D.J. Dobson, S.J. Freeman, P.T. Greenlees, A.N. Qadir, S. Juutinen, J.L. Durell, T. Enqvist, P. Jones, R. Julin, A. Keenan, H. Kettunen, P. Kuusiniemi, M. Leino, P. Nieminen, P. Rahkila, S.D. Robinson, J. Uusitalo and B.J. Varley, Phys. Rev. C **66**, (2002) 064321.

[Dyb83] K. Dybdal, T. Chapuran, D.B. Fossan, W.F. Piel, D. Horn and E.K. Warburton, Phys. Rev. C **28**, (1983) 1171.

[Enq96] T. Enqvist, *thesis*, (Department of Physics, University of Jyväskylä, Research Report No. 3/1996), unpublished.

[Fae84] T. Faestermann, A. Gillitzer, K. Hartel, P. Kienle and E. Nolte, Phys. Lett. **137B**, (1984) 23.

[Fir96] R.B. Firestone and V.S. Shirley, *Table of isotopes, 8th edition*, (Wiley, New York 1996).

[Fot97] N. Fotiades, W. Younes, J.A. Cizewski, D.P. McNabb, K.Y. Ding, C.N Davids, R.V.F. Janssens, D. Seweryniak, M.P. Carpenter, H. Amro, P. Decrock, P. Reiter, D. Nisius, L.T. Brown, S. Fischer, T. Lauritsen, J. Wauters, C.R. Bingham, M. Huyse, A. Andreyev and L.C. Coticchio, Phys. Rev. C **55**, (1997) 723.

[Fre94] S.J. Freeman, A.G. Smith, S.J. Warburton, B.B. Back, I.G. Bearden, D.J. Blumenthal, M.P. Carpenter, B. Crowell, C.N. Davids, D. Henderson, R.V.F. Janssens, T.L. Khoo, T. Lauritsen, C.J. Lister, D.

Nisius, H.T. Penttilä, J.A. Becker, P. Chowdhury and E.F. Moore, Phys. Rev. C **50**, (1994) R1754.

[Ghi88] A. Ghiorso, S. Yashita, M.E. Leino, L. Frank, J. Kalnins, P. Armbruster, J.-P. Dufour and P.K. Lemmertz, Nucl. Instrum. Methods Phys. Res. B **99**, (1988) 192.

[Gil87] A. Gillitzer, T. Faestermann, K. Hartel, P. Kienle and E. Nolte, Z. Phys. A **326**, (1987) 107.

[Gio03] J. Gioviazza, B. Blank, C. Borcea, B.A. Brown, M. Chartier, S. Czajkowski, A. Fleury, R. Grywacz, M. Lewitowicz, M.J. Lopez Jimenez, V. Maslov, F. de Oliveira Santos, M. Pfützner, M.S. Pravikoff, M. Stanoiu and J.-C. Thomas, AIP Conference Proceedings, Vol **681**, Proton-Emitting Nuclei: Second International Symposium, PROCON 2003, (2003) 111.

[Gre53] Alex. E.S. Green and Nicholas. A. Engler, Phys. Rev. **91**, (1953) 40.

[Hau88] P.E. Haustein ed., At. Data Nucl. Data Tables **39**, (1988) 185.

[Hei95] P. Heikkinen and E. Liukkonen, Proceedings of the 14^{th} International Workshop on Cyclotrons and Their Applications, Cape Town, October 8-13 (1995) (World Scientific, Singapore), p. 66.

[Hel99] K. Helariutta, J.F.C. Cocks, T. Enqvist, P.T. Greenlees, P. Jones, R. Julin, S. Juutinen, P. Jämsen, H. Kankaanpää, H. Kettunen, P. Kuusiniemi, M. Leino, M. Muikku, M. Piiparinen, P. Rahkila, A. Savelius, W.H. Trzaska, S. Törmänen, J. Uusitalo, R.G. Allatt, P.A. Butler, R.D. Page and M. Kapusta, Eur. Phys. J. A **6**, (1999) 289.

[Heß89] F.P. Heßberger, S. Hofmann, G. Münzenberg, K.-H. Schmidt, P. Armbruster and R. Hingmann, Nucl. Instrum. Methods A**274**, (1989) 522.

[Hey83] K. Heyde, P. Van Isacker, M. Waroquier, J.L. Wood and R.A. Meyer, Phys. Rep. **102**, (1983) 291.

[Hof82] S. Hofmann, W. Reisdorf, G. Münzenberg, F.P. Heßberger, J.R.H. Schneider and P. Armbruster, Z. Phys. A **305**, (1982) 111.

[Hof84] S. Hofmann, Y.K. Agarwal, P. Armbruster, F.P. Heßberger, P.O. Larsson, G. Münzenberg, K, Poppensieker, W. Reisdorf, J.R.H. Schneider and H.J. Schött, in Proceedings, 7th Int. Conf. on Atomic Mass and Fundamental Constants, Darmstadt-Seeheim, ed. O. Klepper, THD-schriftenreihe Wissenschaft und Technik, (1984) Darmstadt.

[Hof93] S. Hofmann, in Alpha, Proton and Heavy Ion Radioactivities (Particle Emission from Nuclei II), ed. D.N. Poenaru, M.S. Ivascu, Boca Raton: Chemical Rubber Company (1989) 25.

[Hor81] D. Horn, C. Baktash, and C.J. Lister, Phys. Rev. C **24**, (1981) 2136.

[Hua76] Keh-Ning Huang and Hans Mark, At. Data Nucl. Data Tables **18**, (1976) 243.

[Hür02] A. Hürstel, M. Rejmund, E. Bouchez, P.T. Greenlees, K. Hauschild, S. Juutinen, H. Kettunen, W. Korten, Y. Le Coz, P. Nieminen, Ch. Theisen, A.N. Andreyev, F. Becker, T. Enqvist, P.M. Jones, R. Julin, H. Kankaanpää, A. Keenan, P. Kuusiniemi, M. Leino, A.-P. Leppänen, M. Muikku, J. Pakarinen, P. Rahkila and J. Uusitalo, Eur. Phys. J. A **15**, (2002) 329.

[Hür] A. Hürstel, *et al*, to be published.

[Igo58] George Igo, Phys. Rev. Lett. **1**, (1958) 72.

[Jac70] K.P. Jackson, C.U. Cardinal, H.C. Evans, N.A. Jelley and J. Cerny, Phys. Lett. **33B**, (1970) 281.

[Jon95] P. Jones, Ph. D. thesis, University of Liverpool, September 1995 (unpublished).

[Jul01] R. Julin, K. Helariutta and M. Muikku, J. Phys. G: Nucl. Part. Phys. **27**, (2001) R109.

[Ket01a] H. Kettunen, P.T. Greenlees. K. Helariutta, P. Jones, R. Julin, S. Juutinen, P. Kuusiniemi, M. Leino, M- Muikku, P. Nieminen and J. Uusitalo, Acta Phys. Pol. B **32**, (2001) 989.

[Ket01b] H. Kettunen, J. Uusitalo, M. Leino, P. Jones, K. Eskola, P.T. Greenlees, K. Helariutta, R. Julin, S. Juutinen, H. Kankaanpää, P. Kuusiniemi, M. Muikku, P. Nieminen and P. Rahkila Phys. Rev. C **63**, (2001) 044315.

[Ket03] H. Kettunen, S. Eechaudt, T. Enqvist, T. Grahn, P.T. Greenlees, P. Jones, R. Julin, S. Juutinen, A, Keenan, P. Kuusiniemi, M. Leino, A.-P. Leppänen, P. Nieminen, J. Pakarinen, C. Scholey, and J. Uusitalo, AIP Conference Proceedings, Vol **681**, Proton-Emitting Nuclei: Second International Symposium, PROCON 2003, (2003) 26.

[Kle82] O. Klepper, T. Batsch, S. Hpfmann, R. Kirchner, W. Kurcewicz, W. Reisdorf, E. Roeckl, D. Schardt and G. Nyman, Z. Phys. A **305**, (1982) 125.

[Koi94] H. Koivisto, J. Ärje and M. Nurmia, Nucl. Instrum. Methods Phys. Res. B **94**, (1994) 291.

[Koi01] H. Koivisto, P. Heikkinen, V. Hänninen, A. Lassila, H. Leinonen, V. Nieminen, J. Pakarinen, J. Ärje and E. Liukkonen Nucl. Instrum. Methods Phys. Res. B **174**, (2001) 379.

[Kra88] Kenneth S. Krane, *Introductory nuclear physics*, Wiley New York 1998.

[Lac00] M. Lach, P. Bednarczyk, P.T. Greenlees, K. Helariutta, P. Jones, R. Julin, S. Juutinen, H. Kankaanpää, H. Kettunen, P. Kuusiniemi, M. Leino, W. Męczyński, M. Muikku, P. Nieminen, P. Rahkila, J. Styczeń and J. Uusitalo, Eur. Phys. J. A **9**, (2000) 307.

[Lei95a] M. Leino, J. Äystö, T. Enqvist, P. Heikkinen, A. Jokinen, M. Nurmia, A. Ostrowski, W.H. Trazaska, J. Uusitalo, P. Armbuster and V. Ninov, Nucl. Instrum. Methods B **99**, (1995) 653

[Lei95b] M. Leino, J. Äystö, T. Enqvist, A. Jokinen, M. Nurmia, A. Ostrowski, W.H. Trzaska, J. Uusitalo, K. Eskola, P. Armbruster and V. Ninov, Acta Physica Polonica B **26**, (1995) 309.

[Lir76] S. Liran and N. Zeldes, At. Data Nucl. Data Tables **17**, (1976) 431.

[Liu92] Esko Liukkonen, New Cyclotron at Jyväskylä, invated talk at the 13^{th} International Conference on Cyclotrons and Their Applications, Vancouver 1992 (World Scientific, Singapore), p. 22.

[Liv93a] K. Livingston, P.J. Woods, T. Davinson, N.J. Davis, S. Hofmann, A.N. James, R.D. Page, P.J. Sellin and C. Shotter Phys. Lett. **312B**, (1993) 46.

[Liv93b] K. Livingston, P.J. Woods, T. Davinson, N.J. Davis, S. Hofmann, A.N. James, R.D. Page, P.J. Sellin and A.C. Shotter Phys. Rev. C **48**, (1993) R2151.

[Mag02] E. Maglione and L.S. Ferreira, Eur. Phys. J. A **15**, (2002) 89.

[Mah02] H. Mahmud, C.N. Davids, P.J. Woods, T. Davinson, A. Heinz, J.J. Ressler, K. Schmidt, D. Seweryniak, J. Shergur, A.A. Sonzogni and W.B. Walters, Eur. Phys. J. A **15**, (2002) 85.

[Mar76] S. Maripuu and K. Way, At. Data Nucl. Data Tables **17**, (1976) i.

[May77] F.R. May, V.V. Pashkevich and S. Frauendorf, Phys. Lett. B **68**, (1977) 113.

[Mos89] M. Moszyński, J.H. Bjerregard, J.J. Gaardhøje, B. Herskind, P. Knudsen and G. Sletten, Nucl. Instrum. Methods A **280**, (1989) 45.

[Mot55] B.R. Mottelson and S.G. Nilsson, Phys. Rev. **99**, (1955) 1615.

[Mui01] M. Muikku, P.T. Greenlees, K. Hauschild, K. Helariutta, D.G. Jenkins, P. Jones, R. Julin, S. Juutinen, H. Kankaanpää, N.S. Kelsall, H. Kettunen, P. Kuusiniemi, M. Leino, C.J. Moore, P. Nieminen, C.D. O'Leary, R.D. Page, P. Rahkila, W. Reviol, M.J. Taylor, J. Uusitalo and R. Wadsworth, Phys. Rev. C **64**, (2001) 044308

[Möl95] P. Möller, J.R. Nix, W.D. Myers and W.J. Swiatecki, At. Data Nucl. Data Tables **59**, (1995) 185.

[Nie01] P. Nieminen, J.F.C. Cocks, O. Dorvaux, P.T. Greenlees, K. Helariutta, P.M. Jones, R. Julin, S. Juutinen, H. Kankaanpää, H. Kettunen, P. Kuusiniemi, M. Leino, M. Muikku, P. Rahkila, A. Savelius, J. Uusitalo, A. N. Andreyev, F. Becker, K. Eskola, K. Hauschild, M. Houry, M. Huyse, W. Korten, Y. Le Coz, R. Lucas, T. Lönnroth, Ch. Theisen, K. Van de Vel, P. Van Duppen, N. Amzal, P.A. Butler, N. Hammond, C. Scholey and R. Wyss, Acta Physica Polonica B **32**, (2001) 1019.

[Nie03] P. Nieminen, S. Juutinen, A.N. Andreyev, J.F.C. Cocks, O. Dorvaux, K. Eskola, P.T. Greenlees, K. Hauschild, K. Helariutta, M. Huyse P.M. Jones, R. Julin, H. Kankaanpää, H. Kettunen, P. Kuusiniemi, Y. Le Coz, M. Leino, T. Lönnroth, M. Muikku, P. Rahkila, A. Savelius, J. Uusitalo, N. Amzal, N. Hammond, C. Scholey and R. Wyss, to be published.

[Nil55] S.G. Nilsson, Mat. Fys. Medd. Dan. Vid. Selsk. **29**, (1955) No. 16.

[Nov02] Yu. N. Novikov, F. Attallah, F. Bosch, M. Falch, H. Geissel, M. Hausmann, Th. Kerscher, O. Klepper, H.-J. Kluge, C. Kozhuharov, Yu.A. Litvinov, K.E.G. Löbner, G. Münzenberg, Z. Patyk, T. Radon, C. Scheidenberger, A.H. Wapstra and H. Wollnik, Nucl. Phys. A **697**, (2002) 92.

[Oro99] A.M. Oros, K. Heyde, C. De Coster, B. Decroix, R. Wyss, B.R. Barrett and P. Navratil, Nucl. Phys. A **645**, (1999) 107.

[Pag92] R.D. Page, P.J. Woods, R. A. Cunnungham, T. Davinson, N.J. Davis, S. Hofmann, A.N. James, K. Livingston, P.J. Sellin and C. Shotter Phys. Rev. Lett. **68**, (1992) 1287.

[Pag96] R.D. Page, P.J. Woods, R.A. Cunningham, T. Davinson, N.J. Davis, A.N. James, K. Livingston, P.J. Sellin and A.C. Shotter, Phys. Rev. C **53**, (1996) 660.

[Pag03] R.D. Page, A.N. Andreyev, D.E. Appelbe, P.A. Butler, S.J. Freeman, P.T. Greenlees, R.-D.Herzberg, D.G. Jenkins, G.D. Jones, P. Jones, D.T. Joss, R. Julin, H. Kettunen, M. Leino, P. Rahkila, P.H. Regan, J. Simpson, J. Uusitalo, S.M. Vincent and R. Wadsworth, Nucl. Instrum. Methods B **204**, (2003) 634.

[Pau95] E.S. Paul, P.J. Woods, T. Davinson, R.D. Page, P.J. Sellin, C.W. Beausang, R.M. Clark, R.A. Cunningham, S.A. Forbes, D.B. Fossan, A. Gizon, J. Gizon, K. Hauschild, I.M. Hibbert, A.N. James, D.R. LaFosse, I. Lazarus, H. Schnare, J. Simpson, R. Wadsworth and M.P. Waring, Phys. Rev. C **51**, (1995) 78.

[Per57] I. Perlman and J.O. Rasmussen, Alpha Radiactivity, Handbuch der Physik, Band XLII edited by S. Flügge, Springer-Verlag, Berlin-Göttingen-Heidelberg 1957, 109.

[Pfü03] M. Pfützner, E. Badura, C. Bingham, B. Blank, M. Chartier, H. Geissel, J. Giovinazzo, L.V. Grigorenko, R. Grywacz, M. Hellström, Z. Janas, J. Kurcewicz, A.S. Lalleman, C. Mazzocchi, I. Mukha, G. Münzenberg, C. Plettner, E. Roeckl, K.P. Rykaczewski, K. Schmidt, R.S. Simon, M. Stanoiu and J.-C. Thomas, AIP Conference Proceedings, Vol **681**, Proton-Emitting Nuclei: Second International Symposium, PROCON 2003, (2003) 105.

[Pol99] G.L. Poli, C.N. Davids, P.J. Woods, D. Seweryniak, J.C. Batchelder, L.T. Brown, C.R. Bingham, M.P. Carpenter, L.F. Conticchio, T. Davinson, J. DeBoer, S. Hamada, D.J. Henderson, R.J. Irvine, R.V.F. Janssens, H.J. Maier, L. Müller, F. Soramel, K.S. Toth, W.B. Walters and J. Wauters, Phys. Rev. C **59**, (1999) R2979.

[Pol01] G.L. Poli, C.N. Davids, P.J. Woods, D. Seweryniak, M.P. Carpenter, J.A. Cizewski, T. Davinson, A. Heinz, R.V.F. Janssens, C.J. Lister, J.J. Ressler, A.A. Sonzogni, J. Uusitalo and W.B. Walters, Phys. Rev. C **63**, (2001) 044304.

[Rad00] T. Radon, H. Geissel, G. Münzenberg, B. Franzke, Th. Kerscher, F. Nolden, Yu. N. Novikov, Z. Patyk, C. Scheidenberger, F. Attallah, K. Beckert, T. Beha, F. Bosch, H. Eickhoff, M. Falch, Y. Fujita, M. Hausmann, F. Herfurth, H. Irnich, H.C. Jung, O. Klepper, C. Kozhuharov, Yu. A. Litvinov, K.E.G. Löbner, F. Nickel, H. Reich,

W. Schwab, B. Schlitt, M. Steck, K. Sümmerer, T. Winkler and H. Wollnik, Nucl. Phys. A **677**, (2000) 75.

[Ras59] J.O. Rasmussen, Phys. Rev. **113**, (1959) 1593.

[Ras66] J.O. Rasmussen, Alpha-, Beta- and Gamma-Ray Spectroscopy, Siegbahn, K., Ed., North-Holland, Amsterdam, 1966, 701.

[Ryk99] K. Rykaczewski, J.C. Batchelder, C.R. Bingham, T. Davinson, T.N. Ginter, C.J. Gross, R. Grzywacz, M. Karny, B.D. MacDonald, J.F. Mas, J.W. McConnell, A. Piechaczek, R.C. Slinger, K.S. Toth, W.B. Walters, P.J. Woods, E.F. Zganjar, B. Barmore, L.Gr. Ixaru, A.T. Kruppa, W. Nazarewicz, M. Rizea and T. Vertse, Phys. Rev. C **60**, (1999) 011301.

[Sch84] K.-H. Schmidt, C.-C. Sahm, K. Pielenz and H.-G. Clerc, Z. Phys. A **316**, (1984) 19.

[Sch00] K.-H. Schmidt, Eur. Phys. J. A **8**, (2000) 141.

[Sew99] D. Seweryniak, J. Uusitalo, M.P. Carpenter, D. Nisius, C.N. Davids, C.R. Bingham, L.T. Brown, L. Conticchio, C.J. Henderson, R.V.F. Janssens, W.B. Walters, J. Wauters, and P.J. Woods, Phys. Rev. C **60**, (1999) 031304.

[Sim86] R.S. Simon, K.-H. Schmidt, F.P. Heßberger, S. Hlavac, M. Housek, G. Münzenberg, H.-G. Clerc, U. Gollerthan and W. Schwab, Z. Phys. A **325**, (1986) 197.

[Smi03] N.A. Smirnova, P.-H. Heenen and G. Neyens, Phys. Lett. B **569**, (2003) 151.

[Smi99] M.B. Smith, R. Chapman, J.F.C. Cocks, O. Dorvaux, K. Helariutta, P. Jones, R. Julin, S. Juutinen, H. Kankaanpää, H. Kettunen, P. Kuusiniemi, Y. Le Coz, M. Leino, D.J. Middleton, M. Muikku, P. Nieminen, P. Rahkila, A. Savelius and K.-M. Spohr, Eur. Phys. J. A **5**, (1999) 43.

[Sjo76] T.P. Sjoreen, G. Schatz, S.K. Bhattacherjee, B.A. Brown, D.B. Fossan and P.M.S. Lesser, Phys. Rev. C **14**, (1976) 1023.

[Sjo81] T.P. Sjoreen, U. Garg and D.B. Fossan, Phys. Rev. C **23**, (1981) 272.

[Sjo82] T.P. Sjoreen, D.B. Fossan, U. Garg, A. Neskakis, A.R. Poletti and E.K. Warburton, Phys. Rev. C **25**, (1982) 889.

[Smi99] M.B. Smith, R. Chapman, J.F.C. Cocks, O. Dorvaux, K. Helariutta, P. Jones, R. Julin, S. Juutinen, H. Kankaanpää, H. Kettunen, P. Kuusiniemi, Y. Le Coz, M. Leino, D.J. Middleton, M. Muikku, P. Nieminen, P. Rahkila, A. Savelius and K.-M. Spohr, Eur. Phys. J. A **5**, (1999) 43.

[Taa61] R. Taagepera and M. Nurmia, Annales academiæ Scientiarum fennicæ, A 78 VI, (1961) 1.

[Tay96] R.B. Taylor, S.J. Freeman, J.L. Durrell, M.J. Leddy, A.G. Smith, D.J. Blumenthal, M.P. Carpenter, C.N. Davids, C.J. Lister, R.V.F. Janssens and D. Seweryniak, Phys. Rev. C **54**, (1996) 2926.

[Tay99] R.B. Taylor, S.J. Freeman, J.L. Durrell, M.J. Leddy, S.D. Robinson, B.J. Varley, J.F.C. Cocks, K. Helariutta, P. Jones, R. Julin, S. Juutinen, H. Kankaanpää, A. Kanto, H. Kettunen, P. Kuusiniemi, M. Leino, M. Muikku, P. Rahkila, A. Savelius and P. T. Greenlees, Phys. Rev. C **59**, (1999) 673.

[Vel02] K. Van de Vel, A.N. Andreyev, R.D. Page, H. Kettunen, P.T. Greenlees, P. Jones, R. Julin, S. Juutinen, H. Kankaanpää, A. Keenan, P. Kuusiniemi, M. Leino, M. Muikku, P. Nieminen, P. Rahkila, J. Uusitalo, K. Eskola, A. Hürstel, M. Huyse, Y. Le Coz, M.B. Smith, P. Van Duppen and R. Wyss, Eur. Phys. J. A. **17**, (2003) 167.

[Wau97] J. Wauters, J. C. Batchelder, C. R. Bingham, D. J. Blumenthal, L. T. Brown, L. F. Conticchio, C. N. Davids, T. Davinson, R. J. Irvine, D. Seweryniak, K. S. Toth, W. B. Walters, P. J. Woods and E. F. Zganjar, Phys. Rev. C **55**, (1997) 1192

[Wei35] C.F. von Weizsäcker, Z. Phys. **96** (1935) 431.

[Woo92] J.L. Wood, K. Heyde, W. Nazarewicz, M. Huyse and P. Van Duppen, Phys. Rep. **215**, (1992) 101.

[Woo97] P.J. Woods, and C.N. Davids, Annu. Rev. Nucl. Part. Sci. **47**, (1997) 541.

[Zie99] J. F. Ziegler, J. P. Biersack and U. Littmark, *The Stopping and Range of Ions in Solids*, new edition, (Pergamon, New York, 1999).

[You95] W. Younes, J.A. Cizewski, H.-Q. Jin, L.A. Bernstein, D.P. McNabb, C.N Davids, R.V.F. Janssens, T.L. Khoo, C.J. Lister, D.J. Blumenthal, M.P. Carpenter, D. Henderson, R.G. Henry, T. Lauritsen, D.T. Nisius, H.T. Penttilä and M.W. Drigert, Phys. Rev. C **52**, (1995) R1723.

[Åbe97] Sven Åberg, Paul B. Semmes and Witold Nazarewicz, Phys. Rev. C **56**, (1997) 1762; **58**, (1998) 3011.

[Ärj90] J. Ärje, V. Nieminen, J. Choinski and T.A. Antaya, in Proceedings of the 10^{th} International Workshop on ECR Ion Sources, CONF-9011136, ORNL, 1-2 November (1990) 343.